Particle Astrophysics at the Galactic Center

by
Elizabeth Todd

A Dissertation Submitted to the Faculty of the

Department of Physics

In Partial Fulfillment of the Requirements
For the Degree of

Doctor of Philosophy

In the Graduate College

The University of Arizona

2 0 1 1

THE UNIVERSITY OF ARIZONA
GRADUATE COLLEGE

As members of the Dissertation Committee, we certify that we have read the dissertation prepared by Elizabeth Todd

entitled Particle Astrophysics at the Galactic Center

and recommend that it be accepted as fulfilling the dissertation requirement for the Degree of Doctor of Philosophy

_____ Date: 4/25/2011
Feryal Ozel

_____ Date: 4/25/2011
J.D. Garcia

_____ Date: 4/25/2011
Joe Giacalone

_____ Date: 4/25/2011
Ke Chiang Hsieh

_____ Date: 4/25/2011
J. Randy Jokipii

Final approval and acceptance of this dissertation is contingent upon the candidate's submission of the final copies of the dissertation to the Graduate College.

I hereby certify that I have read this dissertation prepared under my direction and recommend that it be accepted as fulfilling the dissertation requirement.

_____ Date: 4/25/2011
Dissertation Director: Feryal Ozel

STATEMENT BY AUTHOR

This dissertation has been submitted in partial fulfillment of requirements for an advanced degree at the University of Arizona and is deposited in the University Library to be made available to borrowers under rules of the Library.

Brief quotations from this dissertation are allowable without special permission, provided that accurate acknowledgment of source is made. Requests for permission for extended quotation from or reproduction of this manuscript in whole or in part may be granted by the head of the major department or the Dean of the Graduate College when in his or her judgment the proposed use of the material is in the interests of scholarship. In all other instances, however, permission must be obtained from the author.

SIGNED: Elizabeth Todd

Acknowledgements

The numerical simluations carried out in this work were performed using the supercomputing resources at the University of Arizona.

Dedication

Dedicated to the memory of my father. I am also grateful for my family and friends who have supported and encouraged me throughout this process. To all those who believed I could, thank you.

Table of Contents

List of Figures

List of Figures—*Continued*

List of Figures—*Continued*

List of Tables

Abstract

The presence of turbulence in astrophysical magnetic fields can have a significant effect on the diffusion of particles and, therefore, should be taken into account when performing simulations involving particle propagation. After reviewing the construction of the turbulent magnetic field component, we incorporate this feature in two separate projects. In the first, we consider the possible source(s) of hadronic cosmic rays thought to be responsible for the diffuse TeV γ-ray emission in the vicinity of the Galactic center. Assuming a completely turbulent magnetic field with an average strength of 10-100μG, we find that relativistic protons do not travel far enough to produce γ-rays spatially correlated with the giant molecular clouds, as seen by HESS, when injected into the interstellar medium by a single point source, such as the supermassive black hole Sagittarius A*. Increasing the number of point sources to five does improve the longitudinal extent of the emission but either shows only weak correlation with the molecular gas or highlights the source positions - both pictures are inconsistent with HESS observations. We conclude that protons must be accelerated throughout the Galactic center region via e.g. a second-order Fermi process in order to reproduce the HESS γ-ray map if the magnetic field there is completely turbulent.

Secondly, we examine the possible link between the asymmetric 511keV electron-positron annihilation emission from the inner Galactic disk and hard low mass X-ray binaries (LMXBs). Three different magnetic field configurations were considered: a completely turbulent field, a field in which the turbulent component has equal energy density as the mean component, and a strongly ordered field with little turbulence. Assuming the environment around each LMXB system is the same, we find that the LMXBs alone cannot account for all the positrons necessary to sufficiently fill the region regardless of the particular magnetic field structure chosen. Another transport mechanism (e.g. a galactic wind) in addition to the diffusive motion caused by the magnetic field fluctuations and/or allowing the LMXBs to be embedded in different phases of the interstellar medium is needed for the LMXB picture to remain a viable possibility.

1. Introduction

Turbulence has been an active area of research for many decades. However, a complete "Theory of Turbulence" has yet to be attained. Despite the experimental and theoretical advances that have been made, there are still major holes remaining in the basic understanding of the subject. Many articles about turbulence are fond of relaying the story of Werner Heisenberg who, when asked what he would ask God given the opportunity, is quoted as saying, "When I meet God, I am going to ask him two questions: Why relativity and why turbulence? I really believe he will have an answer for the first." Horace Lamb apparently made a very similar statement, only he substituted 'quantum electrodynamics' for 'relativity'.

Though no one has been able to derive turbulence from first principles, the intense efforts have led to phenomenological turbulence models. It is our intent to apply what is known about turbulence to two problems of astrophysical interest. We will begin in Chapter 2 with a short review of the general theory of turbulence followed by an outline of the method used to incorporate turbulent magnetic fluctuations into the simulations.

In Chapter 3, we examine the first of our issues: the possible source(s) of relativistic protons thought to be responsible for the diffuse γ-ray emission in the inner 2° of the Galaxy as observed by HESS. Because the high energy photon flux seems strongly correlated with the positions of the giant molecular clouds, we devote a section (3.2) to the discussion these structures. Interactions with the environment cause cosmic rays to cool (Section 3.3) and undergoing scattering events with ambient protons produces a particle cascade (Section 3.4). The novel method we use to propagate the cosmic rays is a hybrid exact/statistical approach and is presented in Section 3.5. Three different source distributions were tested: a single particle accelerator (Sagittarius A*, the supermassive black hole at the center of the Milky Way), five point sources spread throughout the Galactic plane and located between giant molecular clouds, and a situation in which protons do not originate from a point source but rather are accelerated throughout the intercloud medium. A comparison of the different models is made in Section 3.6.

We then widen our study of the Galactic center in Chapter 4 and consider the faint electron-positron annihilation line radiation seen by INTEGRAL. Low mass X-ray binaries (LMXBs) have been proposed as the possible production sites for the positrons since the distribution of these objects shows a similar skew towards negative Galactic longitudes as the measured 511keV line flux. After discussing the limits placed on the initial kinetic energies positrons may have when injected into the interstellar medium (Section 4.2), we detail the processes that lead to positron annihilation (Section 4.3) and energy losses (Section 4.4) as the particles diffuse away from their point of origin

and the rates at which these mechanisms occur. A description of the propagation routine is given in Section 4.5 followed by the results of the simulations in Section 4.6. Though the γ-ray emission maps we produce do have features similar to those observed by INTEGRAL, we will see that it is not quite enough to draw a definite conclusion.

We summarize the main points of each project and end with a few closing remarks in Chapter 5.

2. Turbulent Magnetic Fields

Unlike laminar flow, in which the fluid variables vary smoothly in space and time, turbulent flow is characterized by random, chaotic fluctuations. An indication of whether or not a fluid will exhibit turbulent behavior is given by its Reynold's number, defined as $R = LV/\nu$, where L is the characteristic length scale on which the turbulence is created, V is the characteristic velocity, and ν is the fluid viscosity due to internal friction between individual particles. Generally, fluids with high Reynold's numbers are turbulent while those with low Reynold's numbers are laminar.

In a typical Richardson cascade, turbulence is introduced to the system on a large length scale, e.g. by a driving force or obstacle impeding the flow of the fluid, resulting in large eddies. These large eddies are unstable and break apart, transferring their energy to the newly created smaller eddies. This process continues, generating turbulence on smaller and smaller scales, eventually reaching the point where fluid viscosity becomes important. The span of length scales over which smaller eddies are spawned is known as the inertial range. Beyond this is the dissipation range, shorter lengths where inter-particle friction becomes non-negligible, and, theoretically, when the kinetic energy contained in the turbulence is converted to the internal energy of the fluid itself.

In 1941, A.N. Kolmogorov devised a statistical description of turbulence based on just a handful of assumptions. First, though it is reasonable to expect that the large-scale eddies will reflect the geometry of any physical boundaries or obstacles, Kolmogorov proposed that, as the energy cascades down to smaller length scales, this spatial information is lost and the turbulence becomes isotropic. Therefore, the particular manner in which the turbulence is created becomes unimportant — the characteristics of the eddies depends only on the properties of the fluid. Considering the specific rate of energy dissipation, ϵ, and the viscosity, ν, dimensional analysis reveals that the scale at which viscosity effects become important is given by

$$\eta = \left(\frac{\nu^3}{\epsilon}\right)^{1/4} \tag{2.1}$$

since $[\eta] = \text{length}$, $[\epsilon] = \text{length}^2/\text{time}^3$, and $[\nu] = \text{length}^2/\text{time}$. Eddies whose sizes, r, fall well within the inertial range such that $\eta \ll r \ll L$, where L is the characteristic length of the large eddies, are shielded from knowledge of the means by which the turbulence was generated at large scales and the viscous dissipation at small scales. Defining the wavenumber as $k = 2\pi/r$, the specific energy per wavenumber, u, should only depend on ϵ and k. By again using dimensional analysis, Kolmogorov found that

$$u = C\epsilon^{2/3}k^{-5/3} \tag{2.2}$$

where C is a universal constant and $[u] = \text{length}^3/\text{time}^2$.

Though not derived from first principles, Kolmogorov's "-5/3 rule" has nevertheless been physically observed. One of the earliest confirmations of Equation 2.2 came from an experiment carried out by Grant, Stewart, and Moilliet (1962) in the Discovery Passage, a tidal channel on the west coast of Canada. By towing a probe behind a ship, they were able to measure the downstream component of the water's turbulent velocity. A log-log plot of specific energy per wavenumber, u, versus wavenumber, k, yielded an unmistakably straight line of slope $-5/3$ extending over two orders of magnitude in k.

Later, Champagne (1978) collected data from two field sites (named GUMBO, in Minnesota, and FSII, in Denmark) of the atmospheric boundary layer and, combined with measurements from a variety of experiments carried out by others ranging from isotropic grid flows to cylinder wake flows to axisymmetric jets (see Champagne 1978 for a complete list and references), created composite plots from which several interesting conclusions were drawn. First, though isotropy is one of the key assumptions of Kolmogorov's theory leading to the $-5/3$ rule, the appearance of a Kolmogorov-like $-5/3$ spectrum does not guarantee isotropy. This was evident from plots of axisymmetric jet data which produced a spectral slope of $-5/3$ spanning 3 orders of magnitude in k though analysis revealed the flow to be locally anisotropic. Second, in flows with low Reynold's numbers, no inertial subrange was evident. However, flows with high Reynold's numbers all had similar spectral shapes, regardless of the method by which the turbulence was produced. Champagne therefore concluded that Kolmogorov's $-5/3$ rule applies to flows where the Reynold's number is "sufficiently large".

Kolmogorov's theory is not limited to turbulence on geophysical scales however. Observations made by the XMM-Newton satellite of the intra-cluster medium of the Coma galaxy cluster indicate pressure variations consistent with Kolmogorov-type turbulence with an inertial scale ranging from ∼40-90 kiloparsecs (Schuecker et al. 2004). The magnetic field power spectrum of the north lobe of the Hydra A cluster also follows a -5/3 power law over almost an order of magnitude in wavenumber corresponding to physical lengths of ∼0.3-3kpc (Vogt & EnBlin 2005). Closer to home, studies of the inner solar wind (0.3 - 1AU) by the Helios spacecraft show density and magnetic field amplitude fluctuations in accordance with Equation 2.2 (Marsch & Tu 1990).

What is perhaps even more amazing is that Kolmogorov-like turbulence appears on quantum scales as well. Mauer & Tabeling (1998) experimented with Helium IV, in both the normal and superfluid phases, driven by two counter-rotating disks. The energy spectra obtained at three different temperatures ($1.4\text{K} \leq T \leq 2.3\text{K}$), keeping all other conditions the same, were nearly identical and clearly described by a power-law with exponent -5/3. The good agreement between their experiment and a numerical simulation of the non-linear Schrödinger equation (also known as the Gross-

Pitaevskii equation, a description of the flow of superfluids at low temperatures) by Nore, Abid, and Brachet (1997) led Mauer & Tabeling to suggest that the existance of an inertial range is not a property specific to the Navier-Stokes equations used to describe classical fluid flows.

Soon after, Skrbek, Niemela, & Donnelly (2000) experimented with Helium II, chosen for its extremely low viscosity thereby making very high Reynold's numbers possible in small-scale laboratory experiments. Turbulence was introduced by towing a grid through the HeII, kept at temperatures $1.2\text{K} \leq T \leq 2\text{K}$, and the decay of the vorticity, ω, as a function of time, t, was plotted. Though the amount of fluid in the normal phase (i.e. not in the superfluid phase) relative to the total was varied by a factor of 10, it was found that the vorticity decay could be very well described by the classical spectral model. A fit to the data gives the relationship $\omega \propto t^{-1.1}$ - an exponent very similar to that obtained in wind tunnel experiments.

As noted above, astrophysical magnetic fields can be found in dynamically active regions and are therefore subject to becoming turbulent themselves. This is certainly true near the Galactic Center where we will be focusing our attention. We will therefore use the method developed by Giacalone & Jokipii (1994) to generate the turbulent component of the magnetic fields present in our simulations. The total field can be written as the superposition of a large-scale ordered field, $\mathbf{B}_0$, with a turbulent field, $\delta\mathbf{B}$, which is not necessarily small. By defining the fluctuating field as the sum over a number of plane waves with random polarizations and randomly oriented wavevectors, $\mathbf{k}$, Giacalone & Jokipii created fully three-dimensional turbulence that also obeys Gauss's Law, $\nabla \cdot \mathbf{B} = 0$. For the case of a static, i.e. time-independent, magnetic field, the expression for $\delta\mathbf{B}$ is

$$\delta\mathbf{B}(\mathbf{r}) = \sum_k B_k \left[\cos\alpha_k \hat{\mathbf{x}}' \pm i \sin\alpha_k \hat{\mathbf{y}}'\right] \exp[ikz' + i\beta_k] \tag{2.3}$$

where α_k and β_k are random numbers between 0 and 2π. The primed and unprimed coordinate systems are related by the rotation matrix

$$\mathbf{r}' = \begin{pmatrix} \cos\theta\cos\phi & \cos\theta\sin\phi & -\sin\theta \\ -\sin\phi & \cos\phi & 0 \\ \sin\theta\cos\phi & \sin\theta\sin\phi & \cos\theta \end{pmatrix} \mathbf{r} \tag{2.4}$$

which corresponds to a counterclockwise rotation about the z' axis by ϕ followed by a clockwise rotation about the y' axis by θ. Each wavevector, $\mathbf{k}$, is uniquely determined by two angles, $-1 \leq \cos\theta \leq 1$ and $0 \leq \phi \leq 2\pi$, randomly assigned such that all orientations of the primed coordinates relative to the lab coordinates are equally likely. Thus, from Equation 2.3, we can see that the turbulent component of the magnetic field is formed by overlapping many individual fields whose wavevectors point along the z' axis in their respective coordinate systems and Equation 2.4 describes how each rotated coordinate system relates to the lab frame.

The turbulent energy density spectrum is constructed through the following scaling relation

$$B(k) = B(k_{min}) \left(\frac{k}{k_{min}} \right)^{-\Gamma/2} \tag{2.5}$$

where setting $\Gamma = 5/3$ gives Kolmogorov turbulence. $k_{min} = 2\pi/\lambda_{max}$ is the wavevector corresponding to the longest turbulent wavelength. Note that this expression is true when the k's are evenly spaced linearly between k_{min} and k_{max} since $B^2(k) \propto k^{-\Gamma} dk$. If the k's are evenly spaced on a logarithmic scale, as is often done, then Equation 2.5 should be modified to reflect that $B^2(k) \propto k^{-\Gamma}\, k\, d(\log k)$ i.e. $B^2(k) \propto k^{-\Gamma+1} d(\log k)$.

To calculate the value of $B(k_{min})$ needed in the above equation, we relate the energy contained in the turbulent field to that in the ordered field via

$$\delta\mathbf{B} \cdot \delta\mathbf{B}^* = 2[\Re(\delta\mathbf{B}) \cdot \Re(\delta\mathbf{B})] = B^2_{k_{min}} \sum_n \left(\frac{k_n}{k_{min}} \right)^{-\Gamma} = \eta B_0^2 \tag{2.6}$$

where we have made the assumption that there are sufficiently many waves that the cross-terms cancel out and also that the magnitudes of the imaginary component and real component are equal (hence the appearance of the factor of 2). The parameter η determines how the total energy is partitioned between the two field components. For example, setting $\eta = 2$ creates a situtation in which there is just as much energy contained in the fluctuations as there is in the mean field. For the total magnetic field energy, we then have

$$B^2_{total} = \delta B^2 + B_0^2 = \left(\frac{\eta}{2} + 1 \right) B_0^2 \tag{2.7}$$

In the case of a completely turbulent field, the energy contained in the turbulent field is simply set to B^2_{tot} in Equation 2.6.

An alternative method for generating magnetic field turbulence is to use a fast-Fourier transform (FFT) algorithm. The advantage of the FFT technique is that the field is computed only once at the beginning of the simulation. However, the computational memory requirements can be quite significant as the domain of solution is divided into cells and the field components are calculated at each of the vertices of the grid. A related problem is the accuracy of the magnetic field values. Since it is unlikely that a simulated particle will travel from one cell vertex to another vertex, the magnetic field at the position of the particle must either be an interpolation of the surrounding vertex values, in which case $\nabla \cdot \mathbf{B} = 0$ is not respected, or the field is assumed to be constant in the region around each vertex, in which case the field will be discontinuous. When using the Giacalone & Jokipii method, the field is calculated at each point in a particle's trajectory, ensuring Gauss's Law is obeyed and maintaining accuracy, however it can be time-consuming since the sum over many waves must be

done at each step. Regardless, we opt for the Giacalone & Jokipii method, preferring accurate field structure over time-savings.

3. Diffuse TeV Emission at the Galactic Center[1]

3.1. Introduction

Observations of the Galactic Center by the High Energy Stereoscopic System (HESS) reveal diffuse TeV γ-ray emission roughly 2° in extent (Aharonian et al. 2006). Earlier observations of this region led to the discovery of several point-like sources of very-high energy (VHE, > 100GeV) γ-rays such as HESS J1745-290, which is coincident with the position of the supermassive black hole Sagittarius A* (Aharonian et al. 2004), and G0.9+0.1, a supernova remnant/pulsar wind nebula (Aharonian et al. 2005). These two sources are clearly evident in Figure 3.1a. Taking advantage of HESS's sensitivity, it is possible to subtract these point sources thereby obtaining a map of the diffuse emission shown in Figure 3.1b.

Assuming that the processes creating these γ-rays occur near the Galactic center, a latitudinal spread of 0.2° corresponds to a physical height of ≈30pc. This size is similar to that of the giant molecular clouds in the region. CS line emission from these clouds indicate a total mass of $3 - 8 \times 10^7 M_\odot$ contained within $|l| \leq 1.5°$ and $|b| \leq 0.25°$ (see e.g. Tsuboi , Toshihiro, and Ukita 1999). When a contour plot of the CS emission is superimposed on the diffuse TeV map, a definite correlation can be seen. This feature, combined with the high energies detected by HESS, are strong evidence that the γ-rays are produced from the decay of neutral pions created from scatterings of relativistic cosmic rays with ambient protons.

The diffuse γ-ray spectrum in the region $|l| \leq 0.8°$, $|b| \leq 0.3°$ is a power-law distribution, $dN/dE \propto E^{-\Gamma}$, with spectral index $\Gamma = 2.29 \pm 0.07_{stat} \pm 0.20_{sys}$. Since, for a power-law energy distribution, the spectral index of the γ-rays matches that of the parent cosmic ray population, this implies a cosmic ray spectral index ∼2.3 at the Galactic center which is much harder than that measured in the solar neighborhood (2.75). The apparent spectral index disparity can be resolved if one accounts for the fact that cosmic rays escape the Galaxy on an energy-dependent time-scale $t_{esc} \propto E^{-\delta}$, where $\delta \sim 0.4 - 0.6$ (Bhattacharjee 2000). Thus, propagation effects would be less pronounced in regions near the cosmic ray accelerators (i.e. the Galactic center) than in farther regions where the higher energy particles have had an opportunity to escape thereby making the spectrum softer.

A comparison of the γ-ray flux expected from a Galactic center cosmic ray population identical to the local population to the actual measured flux shows that, although there is relatively good agreement for photon energies below 500GeV, there is a clear excess of observed high-energy γ-rays - above 1TeV, the observed flux is 3-9 times

[1]Wommer, E., Melia, F., and Fatuzzo, M., 2008, MNRAS, 387, 987

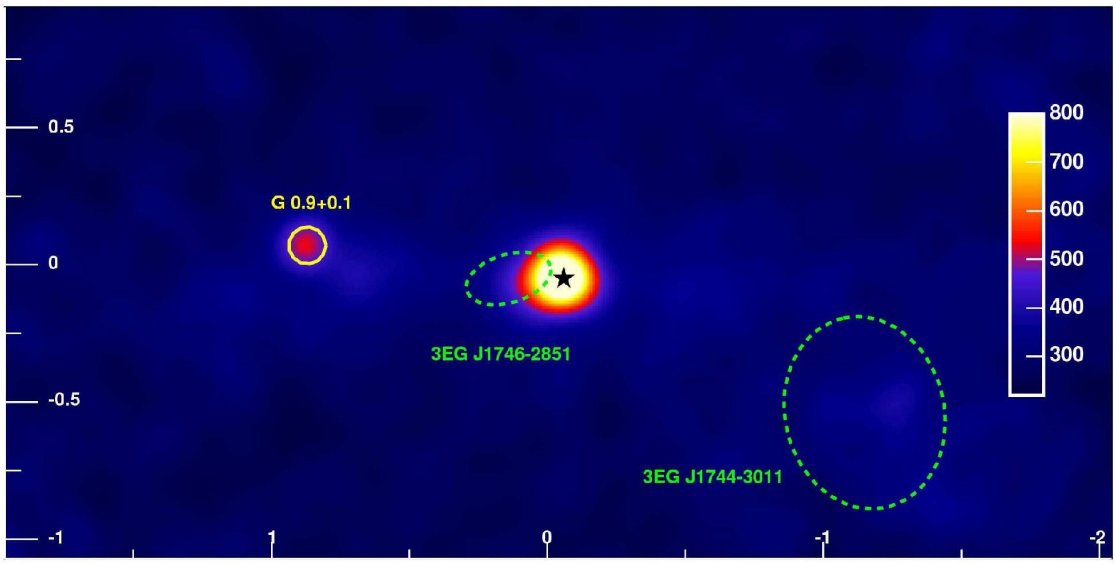

(a) Total γ-ray count map. The x and y axes measure Galactic longitude and latitude, respectively, in degrees. The color scale indicates γ-ray counts. The emission from the two bright sources, G0.9+0.1 and HESS J1745-290, clearly dominates. The green dotted ellipses outline the 95% confidence region for two unidentified EGRET sources. The position of Sagittarius A* is indicated by the black star.

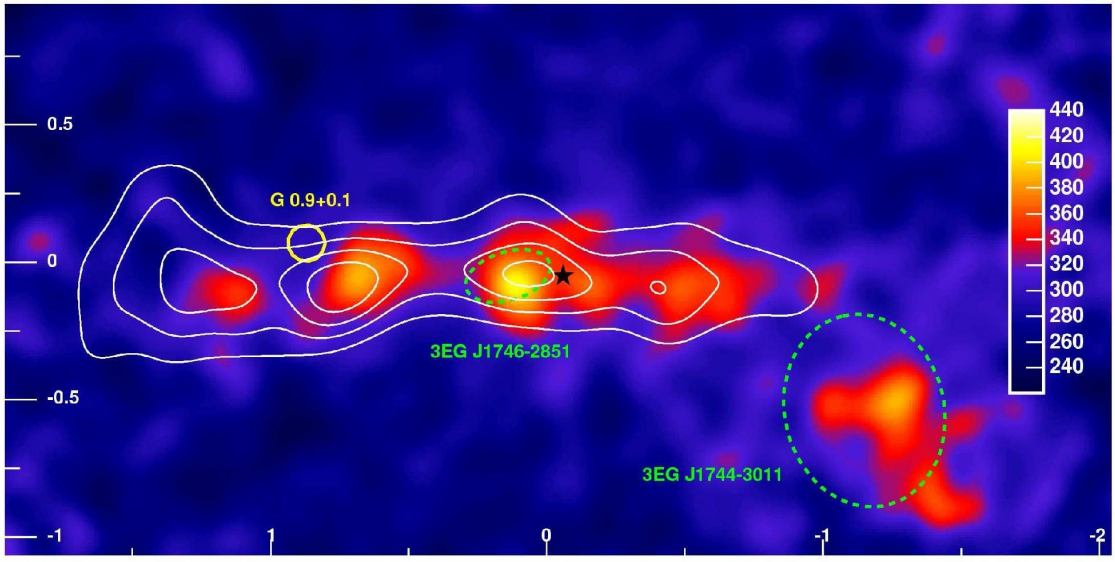

(b) The same map after subtracting the γ-ray contributions from G0.9+0.1 and HESS J1745-290. The white lines are contours of the molecular gas density. The diffuse γ-ray emission appears to be correlated with the gas density. If this is the case, then an interesting feature is the less-than-expected emission from $l \simeq 1.3°$ despite the high density. This suggests that the cosmic rays have not had sufficient time to propagate out to this region and, therefore, must have been accelerated recently.

Figure 3.1: (a–b) — HESS γ-ray maps of the Galactic center (Aharonian et al. 2006).

higher than that predicted by the model (Aharonian et al. 2006). It is reasonable to conclude then that there is also an excess of high-energy cosmic rays in the Galactic center compared to what is measured locally.

In addition, the spectral index of the diffuse emission is nearly identical to HESS J1745-290 implying this object may be the cosmic ray source. The fact that there is relatively little emission at $l = 1.3^\circ$ despite the abundance of target material, coupled with the harder than expected spectrum, suggests that the cosmic rays responsible for the diffuse flux were accelerated recently and have not had sufficient time to propagate beyond $l \sim 1^\circ$. A single SNR within the last 10,000 years, such as Sgr A East, could provide the energy necessary to accelerate cosmic rays up to 10^{15}eV. Another possibility is that the supermassive black hole, Sgr A*, was more active in the recent past.

An alternative explanation is that the diffuse γ-ray flux is due to relativistic electrons inverse-Compton scattering off of ambient photons. However, these electrons would be subject to rapid cooling by the intense photon and magnetic fields in the vicinity of the giant molecular clouds so any such electron accelerator would appear as a point source and have a strong X-ray signature (e.g. G0.9+0.1). Therefore, we will consider only hadronic cosmic ray sources.

In the sections that follow, we will describe the conditions in the Galactic center and the giant molecular clouds through which the relativistic protons will propagate as well as the rates at which these particles cool and scatter when interacting with this environment. In Section 3.5, we describe our technique for simulating the particle motion and end with a discussion of the results of those simulations.

3.2. The Molecular Cloud Distribution

The molecular clouds in the Galactic Center are generally denser, warmer, and more turbulent than those in the disk (Güsten & Philipp 2004). A typical cloud is 50-70 parsecs in size with an average density $n_{H_2} = 10^4$ cm^{-3}. Observations of emissions from density-sensitive molecular species such as CS (Bally et al. 1985), H_2CO (Güsten & Henkel 1983), and HC_3N (Walmsley et al. 1986), however, indicate these clouds are highly nonuniform with high density clumps ($\sim 10^5$ cm^{-3}) embedded in a lower density ($\sim 10^{3.7}$ cm^{-3}) medium. For comparison, the average density of a disk cloud is only $\sim 10^{2.5}$ cm^{-3}.

Estimates of cloud temperatures were first made with measurements of metastable transitions in ammonia (NH_3) and later confirmed with CO line emission observations made by the Antarctic Submillimeter Telescope and Remote Observatory (AST/RO) (see e.g. Kim et al. 2002). Galactic Center clouds are relatively warm (∼30-60K) and the temperatures are fairly uniform (Morris et al. 1983). Collisions with dust resulting in direct heating by energy dissipation had been proposed as a possible heating mechanism but the low temperature of the dust particles (21 ± 2 K) makes this scenario unfeasible (Pierce-Price et al. 2000). Other explanations include magnetic

viscous heating, small-scale dissipation of supersonic turbulence, heating due to the passage of large scale shocks (both J-type, in which the physical conditions across the shock front "jump" instantaneously, and C-type, where the fluid variable vary "continuously" across the shock front), and ultraviolet heating in exposed photodissociation layers. While all of these may contribute on some level, the dissipation of supersonic turbulence remains a front-runner since the heating rate from this process is on par with the cooling rate of the gas.

The magnetic field in the interstellar medium (ISM) lies perpendicular to the plane of the Galaxy. This can be inferred from the strongly polarized synchrotron radiation from the non-thermal filaments (NTFs) which also lie perpendicular to the plane and appear in radio images as long thin strands (Morris 2007). These NTFs show little deformation in encounters with the dense molecular clouds indicating field strengths on the order of a few milliGauss (see e.g. Yusef-Zadeh & Morris 1987). It is not yet clear what the extent of this poloidal field is i.e. whether the NTFs are manifestations of a field that is pervasive throughout the Galactic Center or whether the NTFs are localized structures.

Within the molecular clouds, however, the magnetic field lies parallel to the Galactic plane (Werner et al. 1988) as evidenced by mid- and far-infrared observations of thermal dust emission from magnetically aligned dust grains. An explanation for how the field in the clouds is at right angles to the ISM field is provided by Chuss et al. (2003) who, through far-infrared and sub-millimeter polarimetry observations, determined that the field orientation is linked to the density of the medium. In dense regions, such as the giant molecular clouds, the gravitational energy density becomes greater than the magnetic energy density and the initially poloidal field is sheared into a toroidal configuration. In locations where the matter density is low, such as the ISM, there is insufficient mass to distort the field and it remains poloidal.

How the clouds manage to survive the strong tidal forces in the Galactic Center and remain coherent structures has been a debated question. It has been shown that the virial mass of a molecular cloud scales with its CO luminosity (see e.g. Young & Scoville 1991). The proportionality constant, $X \equiv N(\mathrm{H_2})/I_{CO} = 3.0 \times 10^{20}\mathrm{cm}^{-2}(\mathrm{K\ km\ s}^{-1})^{-1}$, can therefore be used as a conversion factor to estimate a cloud's mass from its CO emission. Oka et al. (1998), however, found that the galactic center clouds do not follow the $L_{CO} - M_{vir}$ trend. Simply changing the value of X is not an option since its value is independently determined by gamma-ray (Blitz et al. 1985) and far-infrared (Cox & Laureijs 1989) observations. From this, Oka et al. (1998) concluded that, instead of being bound by self-gravity, the clouds are in equilibrium with the external environmental pressure. The pressure provided by the surrounding hot plasma, $P_{plasma} \sim 10^{-9.2}$ erg cm^{-3}, is an order of magnitude too small to balance the turbulent pressure within the clouds, $P_{turb} \sim 10^{-8}$ erg cm^{-3} (Güsten & Philipp 2004). If the clouds are bound by their own magnetic fields, then equating the turbulent and magnetic pressures implies field strengths of $\sim$0.5 milliGauss.

Table 3.1: Positions and sizes of GMCs

Cloud	l (°)	b (°)	z_1 (°)	z_2 (°)	Δl (°)	Δb (°)
1	-1.125	-0.375	0.97	-0.04	0.5	0.375
2	-0.75	0.125	1.27	-0.51	0.625	0.25
3	-0.625	0	0.12	2.05	0.5	0.375
4	-0.5	-0.25	-0.38	0.85	0.375	0.375
5	-0.5	0	0.75	0.12	0.5	0.5
6	-0.125	-0.125	0.31	-0.69	0.375	0.125
7	0	0	-0.35	0.39	0.25	0.25
8	0	0	0.15	-1.03	0.625	0.25
9	0.25	-0.25	-0.95	0.85	0.25	0.375
10	0.75	0	-1.22	-0.71	0.625	0.5
11	0.875	-0.125	1.99	0.15	0.5	0.625
12	0.875	0	0.69	0.92	0.75	0.5
13	1.375	0	0.13	-0.42	0.5	0.625
14	2	0	-0.61	1.1	0.375	0.375

The projected positions and sizes of the 14 major giant molecular clouds in the region $|l| \leq 2°$ and $|b| \leq 1°$ were taken from Oka et al. (1998). Each of the clouds listed was rotated about its vertical axis and the resulting ellipsoid was used as the clouds' 3-dimensional shape. A line-of-sight position, z, was randomly assigned to the clouds such that the line-of-sight and longitudinal coordinates had the same angular distribution. Two different sets of z coordinates were used so that our results would not be sensitive to a particular choice of cloud arrangement. Table 3.1 lists the positions and sizes of each of the clouds included in our simulation and Figures 3.2 and 3.3 show the spatial distribution of the clouds for the two different line-of-sight coordinate assignments.

3.3. Energy Loss Rates

If we define the energy-loss rate as

$$R \equiv -\frac{1}{E}\left(\frac{dE}{dt}\right) \tag{3.1}$$

then inelastic collisions with ambient protons of density n_p will cool the relativistic protons at a rate

$$R_{pp} = n_p c \sigma_{pp} K_{pp} \tag{3.2}$$

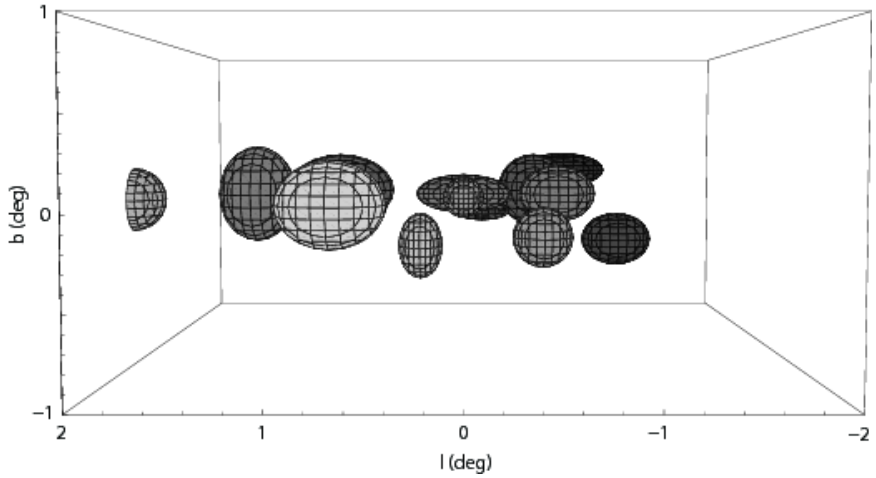

(a)

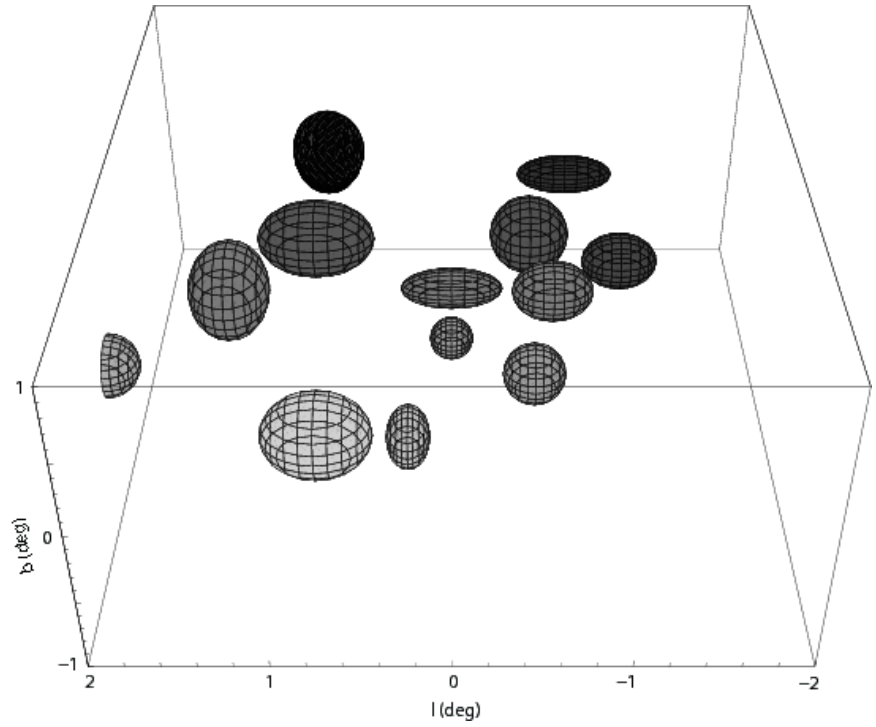

(b)

Figure 3.2: (a–b) — Molecular cloud distribution as viewed from a.) within the Galactic plane and b.) slightly above the plane using the first set of z coordinates.

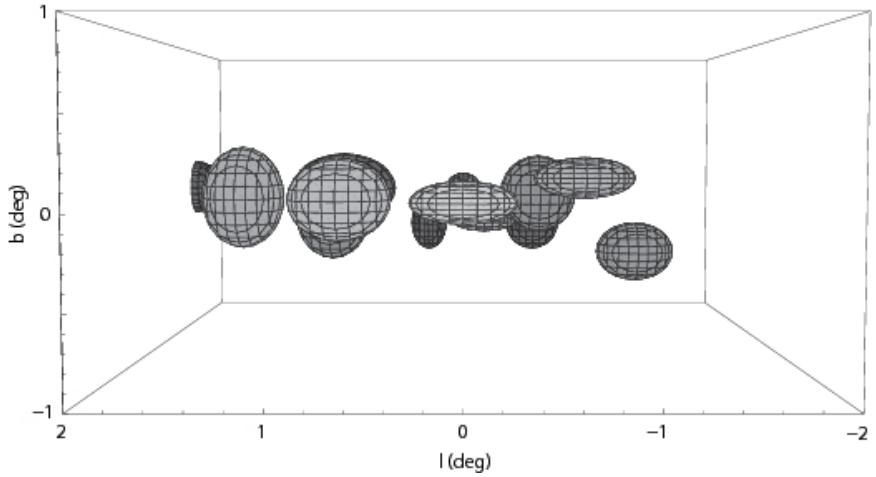

(a)

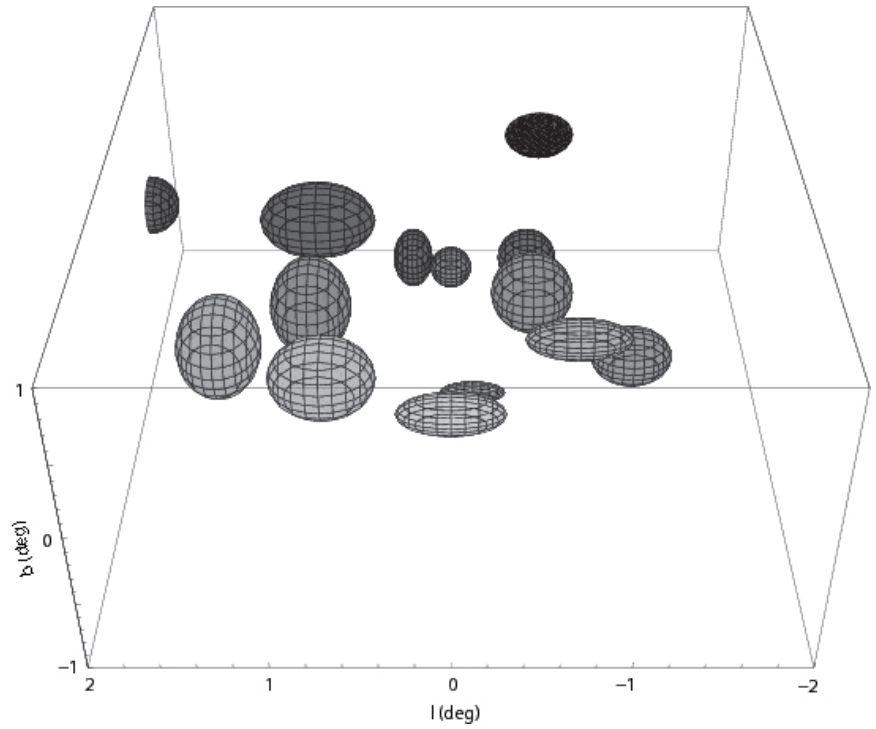

(b)

Figure 3.3: (a–b) — Same as Figure 3.2 except with the second set of z coordinates.

The *pp*-scattering cross-section σ_{pp} has only a weak energy dependence, varying from $\simeq 30$ mbarn for $E_p \sim$ few GeV to 40 mbarn when $E_p \sim 10^3 - 10^4$ GeV (Karol 1988). Similarly, the inelasticity parameter K_{pp} is a function of the center of momentum energy $\sqrt{s}$ with $K_{pp} = 1.35 s^{-0.12}$ for $\sqrt{s} \geq 62$ GeV and $K_{pp} = 0.5$ for $\sqrt{s} \leq 62$ GeV (see Markoff, Melia, & Sarcevic 1997, 1999). Because of this mild energy dependence, we simplify our calculations by assuming constant values of $\sigma_{pp} = 40$ mbarn and $K_{pp} = 0.5$.

An inelastic collision between a high-energy proton and a photon may create an electron/positron pair, $p\gamma \rightarrow pe^+e^-$, or a pion, $p\gamma \rightarrow p\pi^0$ and $p\gamma \rightarrow n\pi^+$. The cross-section and inelasticity for $p\gamma$ scatterings depend on the photon energy (see e.g., Begelman, Rudak, & Sikora 1990) with the threshold photon energy for pair production given by $E_{th}^{'(e)} = 2m_e \sim$1 MeV and for pion production by $E_{th}^{'(\pi)} = m_\pi(1 + m_\pi/2m_p) \sim$145 MeV when measured in the proton rest frame.

Protons will cool via synchrotron radiation at a rate

$$R_{synch} = \frac{4}{3}\left(\frac{m_e}{m_p}\right)^3 \frac{c\sigma_T u_B}{m_e c^2}\gamma_p \tag{3.3}$$

where $u_B = B^2/2\mu_0$ is the magnetic field energy density and σ_T is the Thomson cross-section.

For Compton scattering, the energy-loss rate is given by

$$R_C = \frac{u_{rad}\left[x < \frac{m_p}{m_e}\gamma_p^{-1}\right]}{u_B} R_{synch} \tag{3.4}$$

where u_{rad} is the radiation energy density.

Plots of the above listed cooling rates for both the intra- and inter-cloud environments are shown in Figure 3.4. For all but the highest proton energies, the *pp*-scattering energy losses dominate so, without sacrificing much accuracy, we can further simplify our simulations by ignoring the contributions from $p\gamma$ scattering, synchrotron losses, and Compton scattering.

3.4. The Particle Cascade

The fraction of protons that will undergo a *pp*-scattering after traveling a distance dx can be determined using the expression

$$\frac{dN}{dx} = -N n_H \sigma_{pp} \tag{3.5}$$

where n_H is the number density of ambient protons.

In the event that the *pp*-scattering produces a π^0, the π^0 emissivity is given by

$$Q_{\pi_0}^{pp} = c n_H \int_{E_{th}(E_{\pi^0})} n_p(E_p) \frac{d\sigma(E_{\pi^0}, E_p)}{dE_{\pi^0}} dE_p \tag{3.6}$$

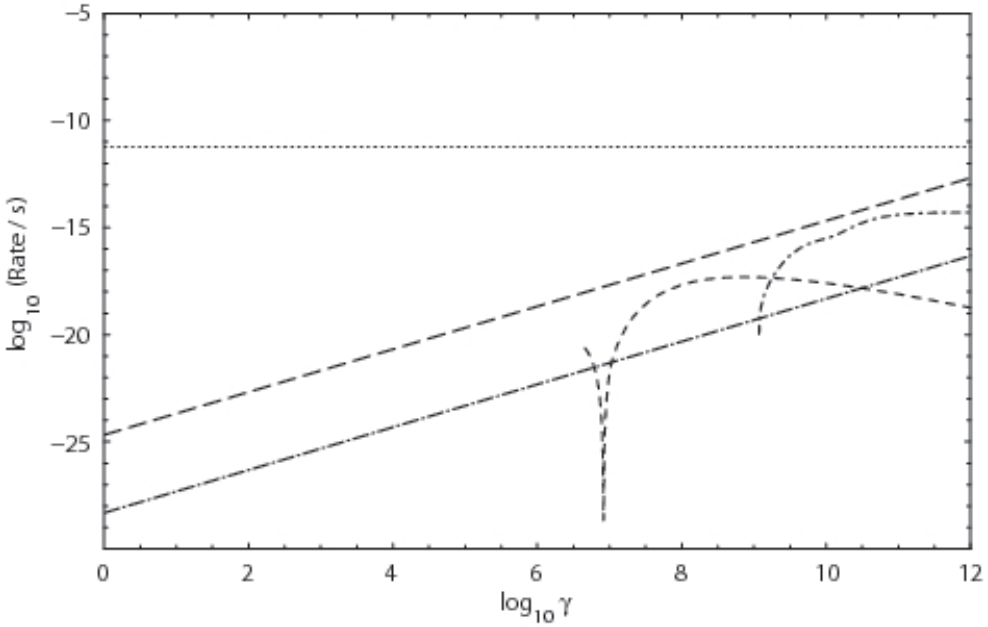

(a)

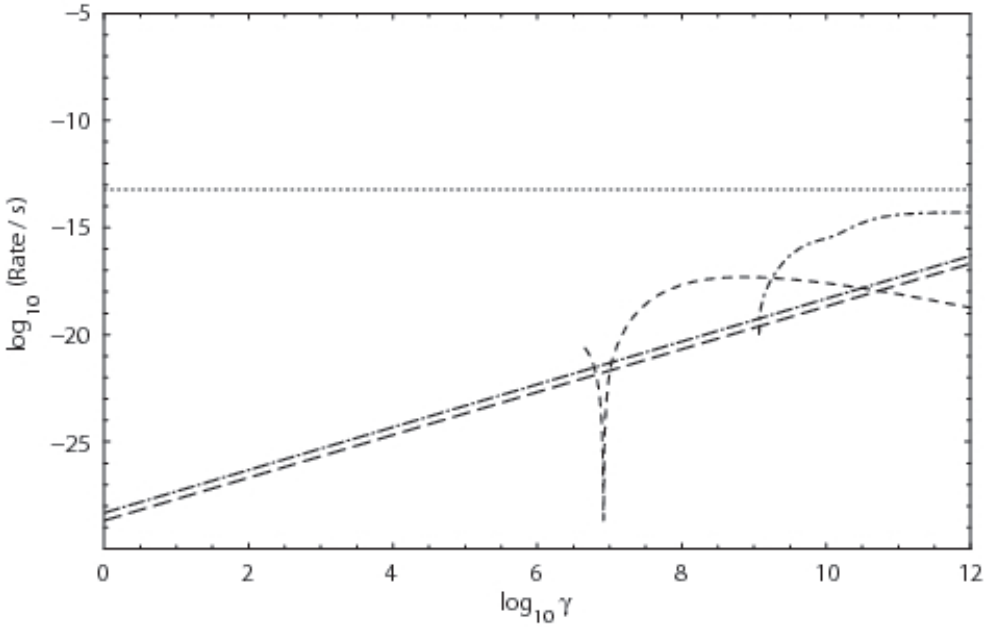

(b)

Figure 3.4: (a–b) — Cooling rates as a funtion of proton Lorentz factor γ for a.) within the molecular clouds and b.) the region between the clouds. The *pp*-scattering energy-loss rate is shown as a dotted line, $p\gamma$ pair production as a short-dashed line, $p\gamma$ pion production as a short-dash-dotted line, synchrotron as a dash-dotted line, and Compton as a long-dashed line.

where the relativistic proton density is $n_p(E_p)$ and $E_{th}(E_{\pi^0})$ is the threshold proton energy for producing a pion with energy E_{π^0}.

When the neutral pion decays, it produces two gamma rays: $\pi^0 \rightarrow 2\gamma$. The resulting gamma-ray emissivity is

$$Q_\gamma(E_\gamma) = 2\int_{E_{\pi^0}(E_\gamma)} \frac{Q_{\pi^0}^{pp}}{\left(E_{\pi^0}^2 - m_{\pi^0}^2 c^4\right)^{1/2}} dE_{\pi^0} \tag{3.7}$$

where $E_{\pi^0}^{min}(E_\gamma) = E_\gamma + m_{\pi^0}^2 c^4/(4E_\gamma)$.

For protons with energies above 7 GeV, the differential π^0 cross-section can be approximated by

$$\frac{d\sigma(E_p, E_{\pi^0})}{dE_{\pi^0}} = \frac{\sigma_0}{E_{\pi^0}} f_{\pi^0}(x) \tag{3.8}$$

where $x = E_{\pi^0}/E_p$, σ_0 =32 mbarn, and

$$f_{\pi^0}(x) = 0.67(1-x)^{3.5} + 0.5e^{-18x} \tag{3.9}$$

accounts for the energy-dependent pion spectrum occuring at high energies (Blasi & Colafrancesco 1999). At low energies (E_p <3 GeV), we use the isobaric model of Stecker (1970) (see also the discussion in Dermer 1986). Because the calculation of the low-energy differential cross-section involves many lengthy expressions, it is not included here but can be found, for example, in the appendix of Fatuzzo & Melia (2003). For proton energies falling between these two regimes (3 GeV < E_p < 7 GeV), we used a linear function connecting the low and high energy cross-section values.

3.5. Proton Propagation

To model the propagation of protons, there are two basic methods:

1. Solving the Lorentz force equation, $\vec{\mathbf{F}} = q\vec{\mathbf{v}} \times \vec{\mathbf{B}}$, for each particle, and
2. solving the diffusion equation,

$$\frac{\partial W}{\partial t} + \frac{\partial}{\partial x_i}(W v_i) - \frac{\partial}{\partial x_i}\left(\kappa_{ij}\frac{\partial W}{\partial x_j}\right) + \frac{\partial}{\partial T}\left(W\frac{\partial T}{\partial t}\right) = 0$$

where $W(x_i, t, T)$ is the distribution function, κ_{ij} is the diffusion coefficient tensor, and T is the kinetic energy.

Calculating the positions of individual protons using the Lorentz force equation from birth to death is incredibly time-consuming. Using the diffusion equation, on the other hand, relies on diffusion coefficients whose values are poorly constrained. In order to both quickly and accurately simulate many particles, we use a two-part

method in which we first collect data on the spatial distribution of protons after a relatively short time and then use the statistics from this short simulation to model the diffusion over a much longer time period.

To generate our particle statistics, we solve the Lorentz force equation for 1000 protons with initial kinetic energy T_p. The total simulation time, τ, is set large enough that the particles undergo many gyrations, yet small enough that the fractional energy loss from beginning to end will be no more than 1% (i.e. $\Delta E/E \leq 0.01$). Because the cooling rate between the giant molecular clouds differs from that within the clouds, τ will be different for the two regions and this process must be done for each environment. For the short simulations, we ignore energy losses (since they are small) and focus solely on particle propagation.

The magnetic field at each point of a proton's trajectory is calculated according to the discussion in Chapter 2. Here we assumed a completely turbulent field with a Kolmogorov spectrum and used 200 values of k evenly spaced on a logarithmic scale with $k_{min} = 2\pi/10r_{gyr}$ and $k_{max} = 2\pi/0.1r_{gyr}$ where $r_{gyr} = \gamma_p m_p v/eB$ is the gyroradius of a proton moving at Lorentz factor γ_p.

To determine the proton's position after a timestep Δt, we transform to a coordinate system in which the total magnetic field points along the $\hat{z}'$ direction, solve the Lorentz force equation, and rotate back to the unprimed lab coordinates. At each step of the trajectory, the Δt is chosen to be some (different) random fraction of the gyroperiod $t_{gyr} = 2\pi\gamma_p m_p/eB$. This process is repeated until the time limit τ has been reached. An example of the particle motion is shown in Figure 3.5.

By recording the final positions of 1000 protons and binning the data, we can determine the probability that a particle will travel a net distance r after time τ (Figure 3.6). For a one-dimensional random walk, along the x-direction for example, the probability density as a function of position, $P(x)$, is proportional to $e^{-(x-x_0)^2/2\sigma_x^2}$. In a three-dimensional random walk, if each direction of motion is independent of the others, then the probability density $P(x, y, z)$ is simply the product of the individual probability densities. The three-dimensional distribution function will then be proportional to $P(x)\,P(y)\,P(z)\,dx\,dy\,dz$. If the motion is isotropic (so that $\sigma_x \sim \sigma_y \sim \sigma_z$), then changing from cartesian to spherical coordinates will give a distribution function proportional to $e^{-(r-r_0)^2/2\sigma^2} r^2 dr$. To fit the data, we used a Gaussian function only:

$$N(r) = N_0 \mathrm{e}^{-(r-\bar{r})^2/2\sigma^2} \tag{3.10}$$

Though the data are not normally distributed (the rising edge is steeper than the trailing end as the distribution function $N(r) \propto r^2 e^{-(r-r_0)^2/2\sigma^2}$ mentioned above would predict), this is an adequate description for our purposes and simplifies the simulation code. $\bar{r}$ and σ are the average distance and standard deviation, respectively. These parameters were determined by using the Levenberg-Marquardt method to minimize the χ^2 function. As one would expect, $\bar{r}$ and σ are functions of the proton energy so this process was repeated for several energies $10^{11}\mathrm{e}V \leq T_p \leq T_{p,trans}$ where $T_{p,trans}$

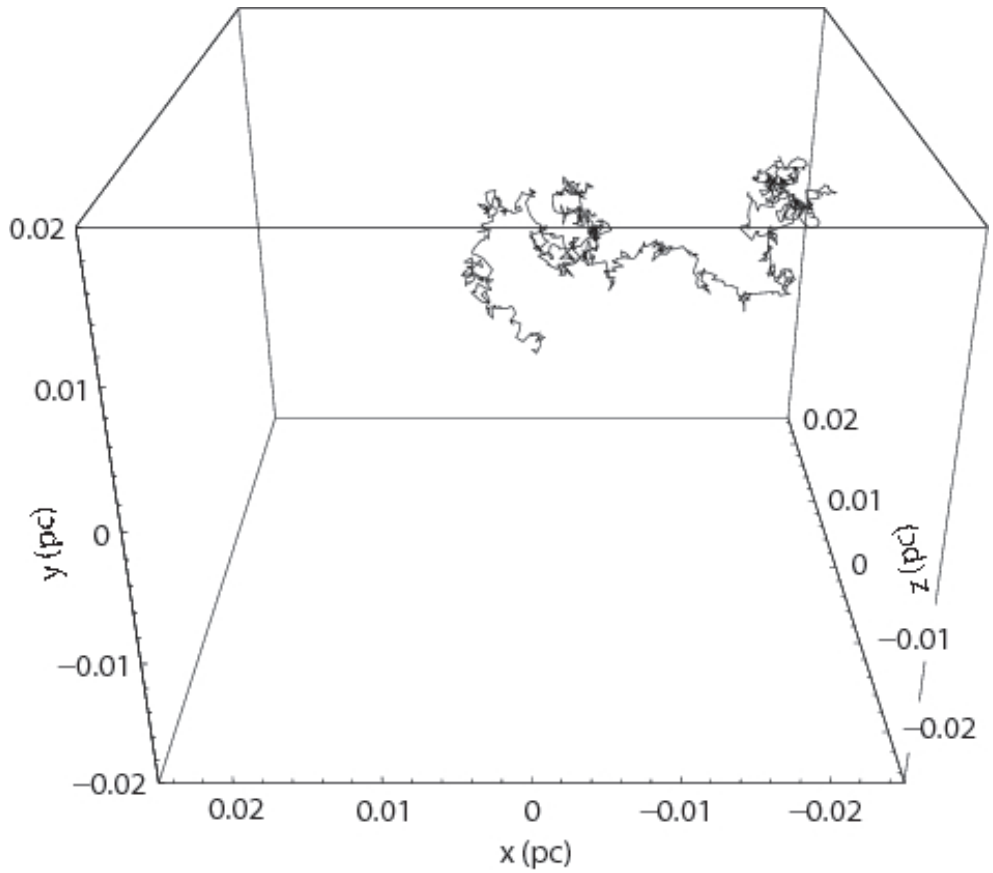

Figure 3.5: Trajectory of a 1 TeV proton for a duration of 3.33×10^8 seconds through a completely turbulent magnetic field. Every 50th step is shown.

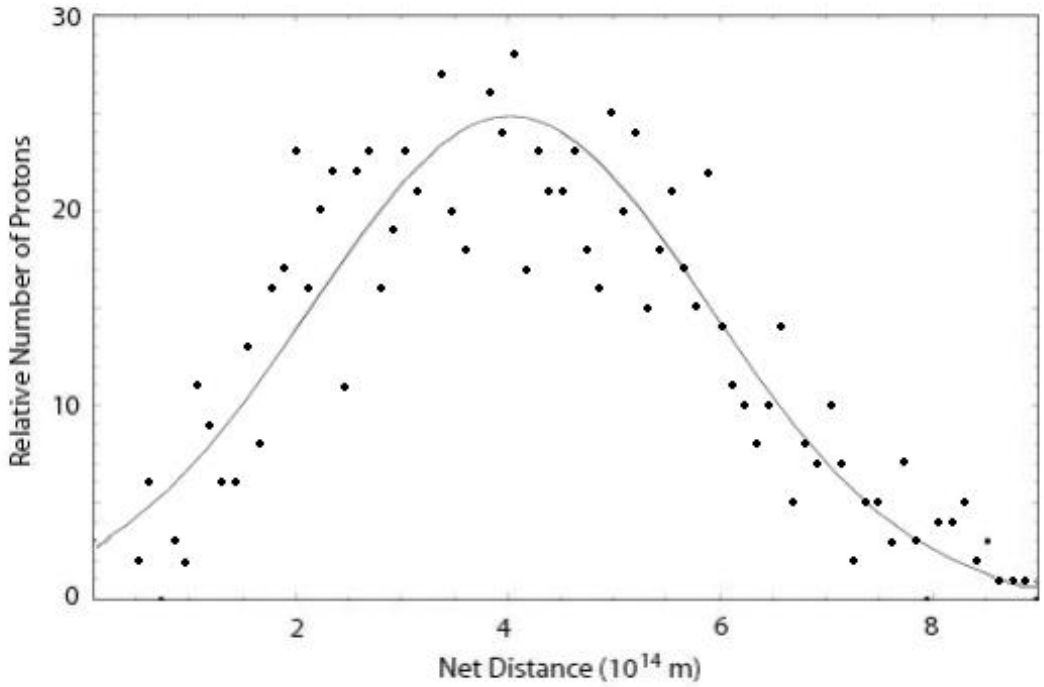

Figure 3.6: Results from a short simulation of 1000 1-TeV protons showing the distribution of particles as a function of net distance traveled after 3.33×10^8 seconds. The line is the Gaussian fit to the data points, where $\bar{r} = 4.05 \times 10^{14}$m and $\sigma = 1.91 \times 10^{14}$m.

is the energy at which the protons transition from diffusive to straight-line motion. We take this point to occur when the total distance covered by the protons in time τ becomes greater than 10 gyroradii.

In terms of the proton energy, $\bar{r}$ and σ can be written as

$$\log\left(\frac{\bar{r}}{1\text{m}}\right) = a_r + b_r \log\left(\frac{T_p}{1\text{eV}}\right) \tag{3.11a}$$

$$\log\left(\frac{\sigma}{1\text{m}}\right) = a_\sigma + b_\sigma \log\left(\frac{T_p}{1\text{eV}}\right) \tag{3.11b}$$

The constants a_r, b_r, a_σ, and b_σ were found by fitting a linear function to the log-log plots of $\bar{r}$ and σ. Table 3.2 shows some calculated values of these fitting coefficients for different combinations of the magnetic field strength, B, and the ambient proton density, n_p.

Table 3.2: Fitting coefficients

B(μG)	n_p(cm^{-3})	τ(s)	a_r	b_r	a_σ	b_σ
10	100	1.67×10^{10}	9.98033	0.499622	9.68435	0.497083
100	100	1.67×10^{10}	9.50314	0.497989	9.16946	0.498592
1000	10^4	1.67×10^9	8.48292	0.499238	8.13816	0.500453

To run the full simulation, Equations 3.11a and 3.11b are combined with Equation 3.10 providing a full description of the probability that a proton of energy T_p will travel a net distance r from its point of origin in a time τ. At each timestep $\Delta t = \tau$, a uniform random number $0 \leq x \leq 1$ is generated which represents a fraction of the normalized area under the $N(r, T_p)$ vs. r curve. Because we have chosen to use a completely turbulent magnetic field, the direction (θ, ϕ) in which the proton propagates is randomly assigned such that $-1 \leq \cos\theta \leq 1$ and $0 \leq \phi \leq 2\pi$ are isotropic distributions. The net distance the proton moves is that value of r with normalized area x to its left. For example, if $x = 0.5$ then the net distance traveled would be $\bar{r}$ since that is the value of r with half the normalized area to its left. After the particle's new position has been found, we then determine the energy lost in time Δt and cool the particle by that amount.

This method allows us to quickly yet accurately simulate the particle motion since the timesteps τ are much larger compared to what we would have used in solving the Lorentz force equation while still reproducing the same spatial distribution. The process is continued until all but 1% of the protons have undergone a scattering event or the proton leaves the volume of solution.

3.6. Results and Discussion

Because the brightest γ-ray source on HESS's map is HESS J1745-290, we begin by assuming that Sagittarius A* is the sole origin of the cosmic rays. Figure 3.7 is the resulting γ-ray contour map calculated using Equations 3.6 and 3.7. The top panel shows the full γ-ray count map and spans eight orders of magnitude transitioning from the most intense (white) to the least intense (blue) emission regions. The diffuse TeV map produced by HESS (Figure 3.1b), however, has only a factor of 2 separating the high and low counts. To make a more direct comparison between our simulation and HESS's observations, we re-map our results with the same factor of 2 count range (bottom panel). It is clear from these plots that Sgr A* alone cannot produce the diffuse emission seen by HESS. Although the central intensity peak may provide an explanation for HESS J1745-290, the γ-rays remaining after the subtraction of this bright spot barely extend to 0.5° and are obviously centered on the location of Sgr A*.

Our second attempt to reproduce the results of the HESS map was to have the

cosmic rays originate from several sources distributed along the Galactic plane. Since HESS's observations indicate there are five TeV "hotspots" in the region $|l| \leq 1.25°$ and $|b| \leq 0.5°$, we placed five distinct cosmic ray sources at the corresponding latitude and longitude coordinates, randomly assigning each a line-of-sight coordinate such that they were positioned in the inter-cloud medium. This simulation was run with two different values for the average magnetic field strength: 10μG (Figure 3.8) and 100μG (Figure 3.9). These plots show that, as the magnetic field strength increases, the motion of the relativistic protons becomes more restricted to the region immediately surrounding their source. In the case of the strong field, the TeV emmission is so concentrated on the cosmic ray origins that all five sources are easily distinguishable and appear equally bright. The weaker field allows the protons to diffuse farther and there is a vague correlation with the molecular clouds, but even this situation does not create the relatively smooth γ-ray emission seen by HESS.

If we maintain that the diffuse γ-ray emission is due to hadronic cosmic ray interactions with the dense material of the giant molecular clouds, then it seems our only recourse is to have the protons accelerated throughout the Galactic center region instead of injected into the medium from point sources. Our final simulation is one in which energetic protons emerge uniformly from the interstellar medium, accelerated via e.g. a second-order Fermi process due to the magnetic field turbulence. The origin of each particle is randomly determined but always falls between molecular clouds. Figure 3.10 shows the resulting γ-ray map when protons are accelerated in this manner. The emission is fairly smooth and highlights the cloud positions quite well.

3.7. Conclusion

For the environmental conditions we have assumed, a point-source origin for the cosmic rays responsible for the diffuse TeV emission at the Galactic center is unlikely. While Sagittarius A* may produce the intense γ-ray flux from HESS J1745-290, the protons do not diffuse far enough to produce the extended emission seen along the plane. Situations involving multiple point sources can increase the longitudinal extent of the emission but these scenarios produce photon maps in which the locations of the sources are clearly evident thereby making them inconsistent with HESS observations. Cosmic rays accelerated throughout the intercloud medium, however, do produce smooth emission correlated with the positions of the giant molecular clouds in the region as required by HESS.

A logical next step to this work would be to explore whether second-order Fermi acceleration in the Galactic center region can produce the hard cosmic ray population responsible for the diffuse emission. An interesting scenario would be a hybrid of the multiple point source and diffuse acceleration alternatives. In an attempt to explain the origin of galactic cosmic rays, Fan (1951) proposed that lighter cosmic rays (such as protons and helium nuclei) are the result of energetic heavier nuclei (ejected by

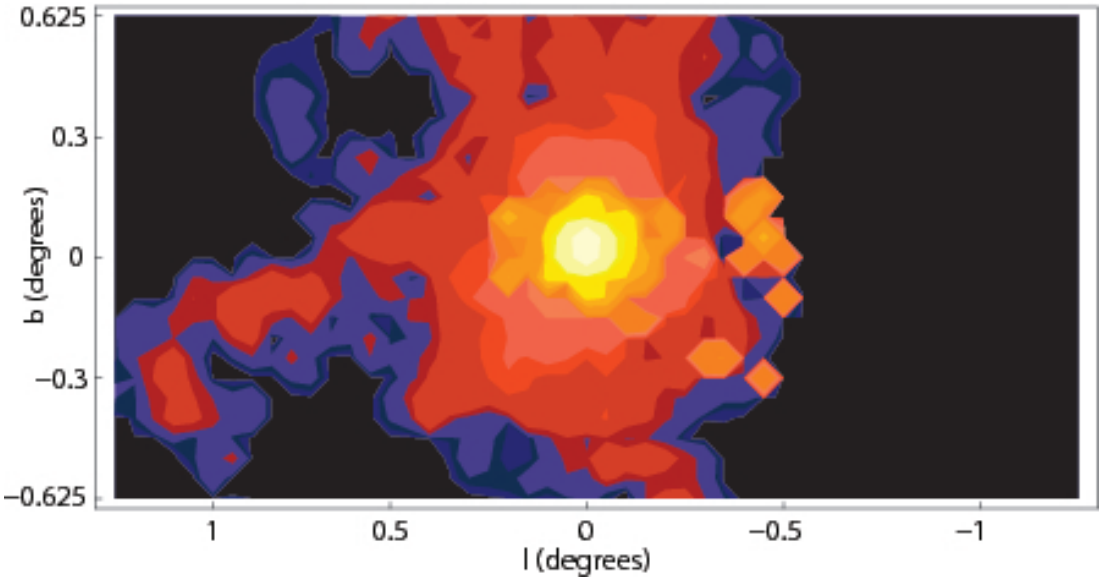

(a)

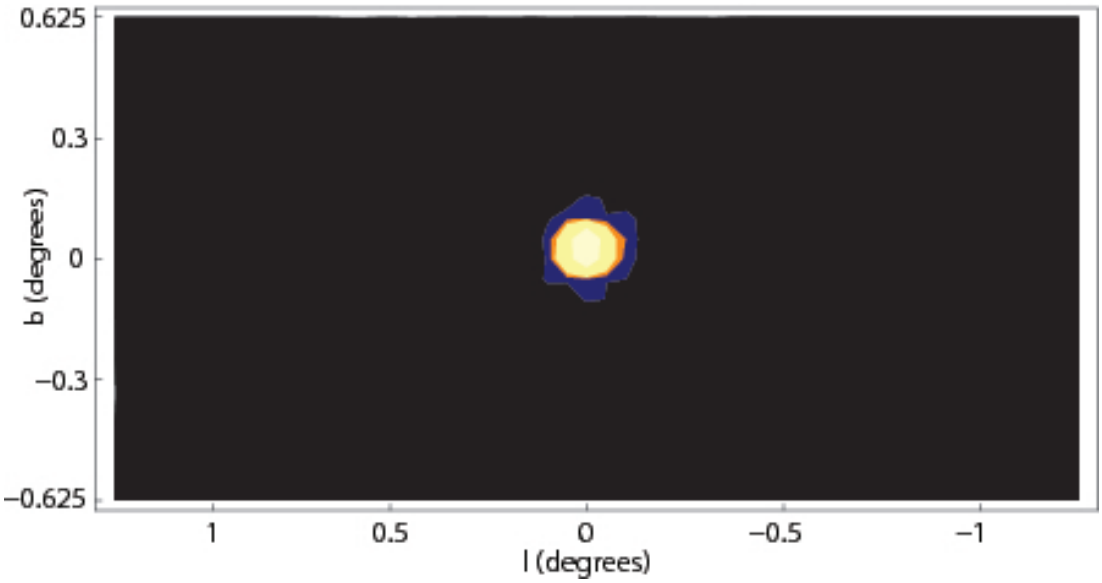

(b)

Figure 3.7: (a–b) — γ-ray emission map (0.2TeV $\leq$ E_γ $\leq$ 10TeV) with Sagittarius A* as the sole source of cosmic rays and an intercloud average magnetic field strength of 10 μG. Top: Full range of γ-ray counts spanning eight orders of magnitude from brightest (white) to dimmest (dark blue) regions. Bottom: Same map, but showing only the most intense emission such that there is only a factor of 2 difference between the bright (white) and dim (blue) regions.

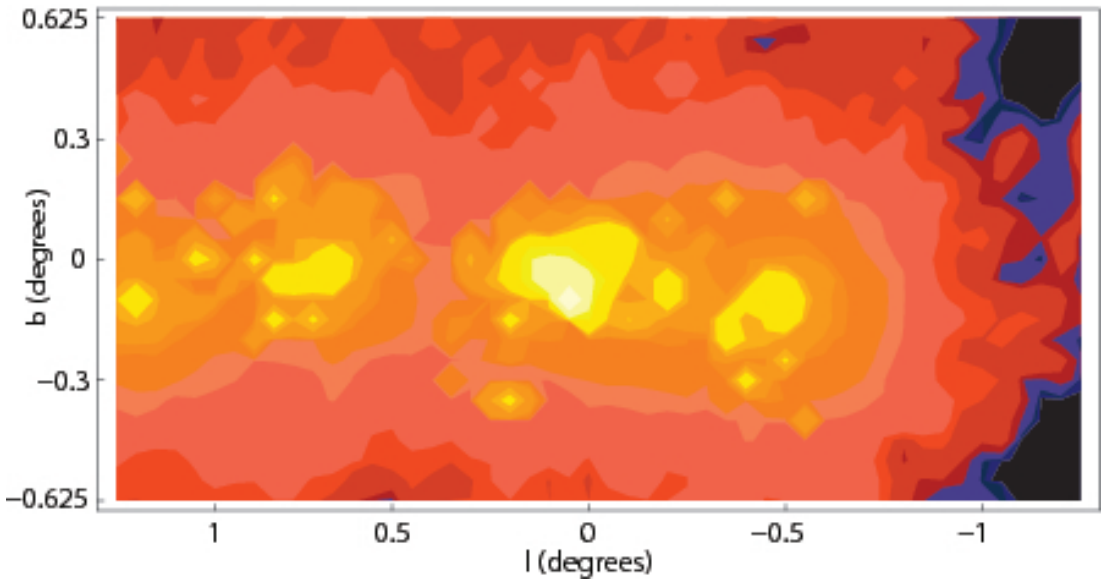

(a)

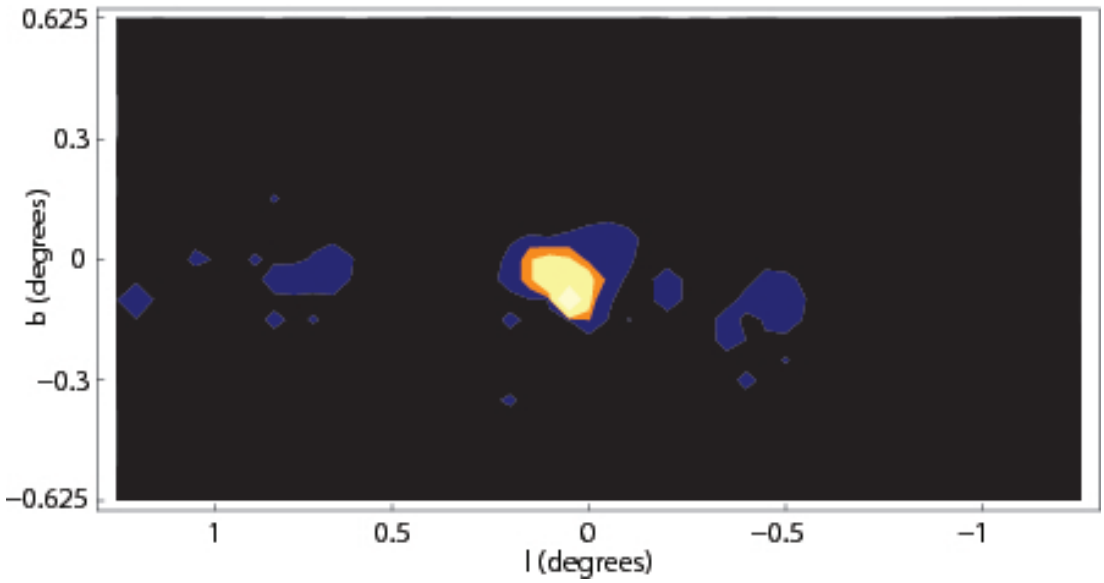

(b)

Figure 3.8: (a–b) — Same as Figure 3.7 except with five cosmic ray sources distributed throughout the Galactic plane, between the molecular clouds. Having multiple sources does increase the extent of the emission though the correlation with the molecular gas is weak.

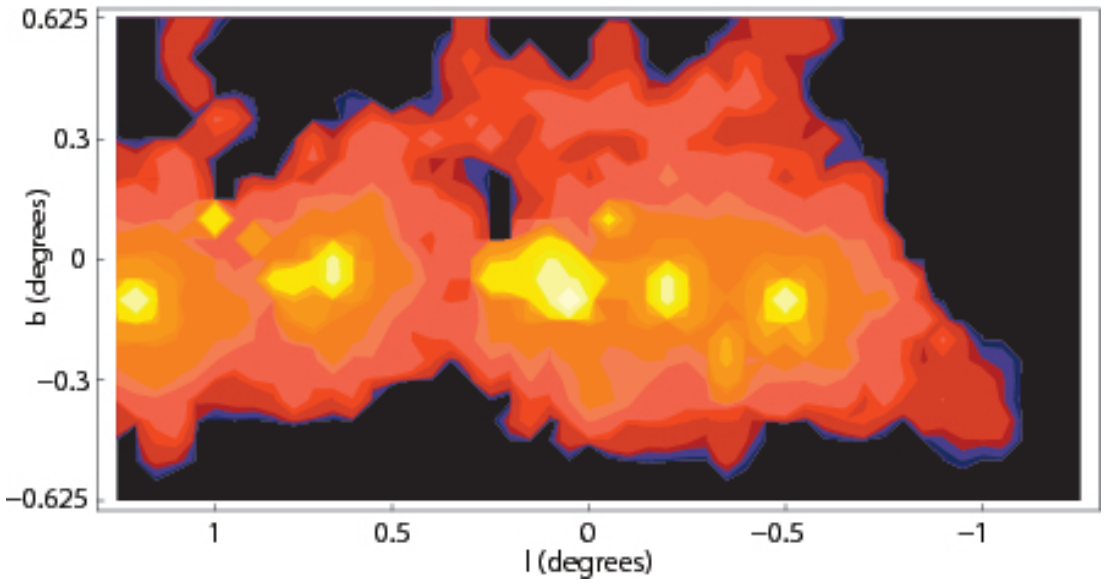

(a)

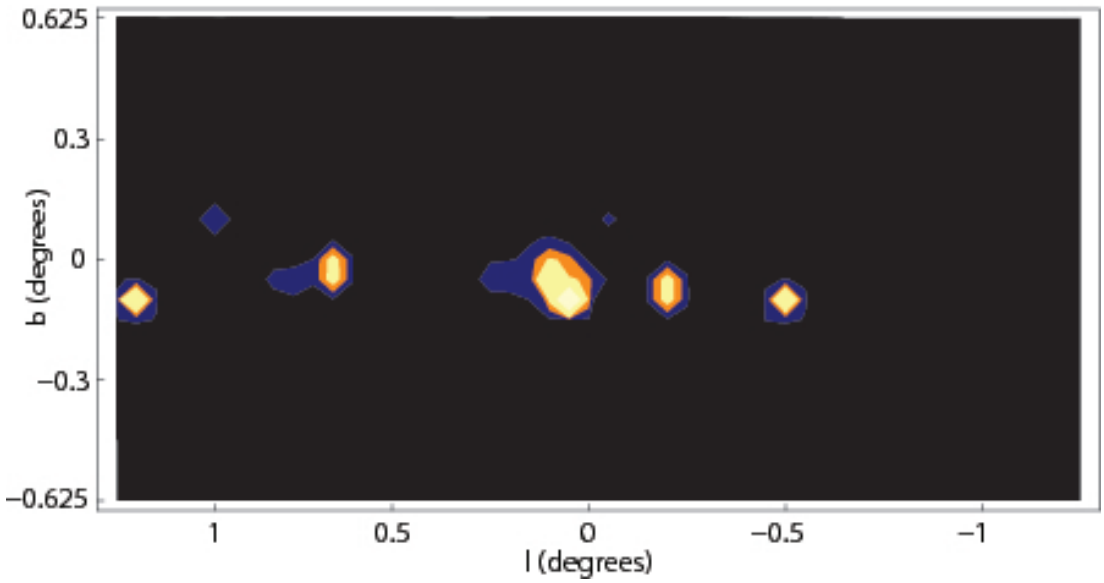

(b)

Figure 3.9: (a–b) — Same as Figure 3.8 but with an average magnetic field strength of 100 μG in the intercloud medium. Because of the stronger magnetic field, the emission is more concentrated around the positions of the cosmic ray sources therefore illuminating them.

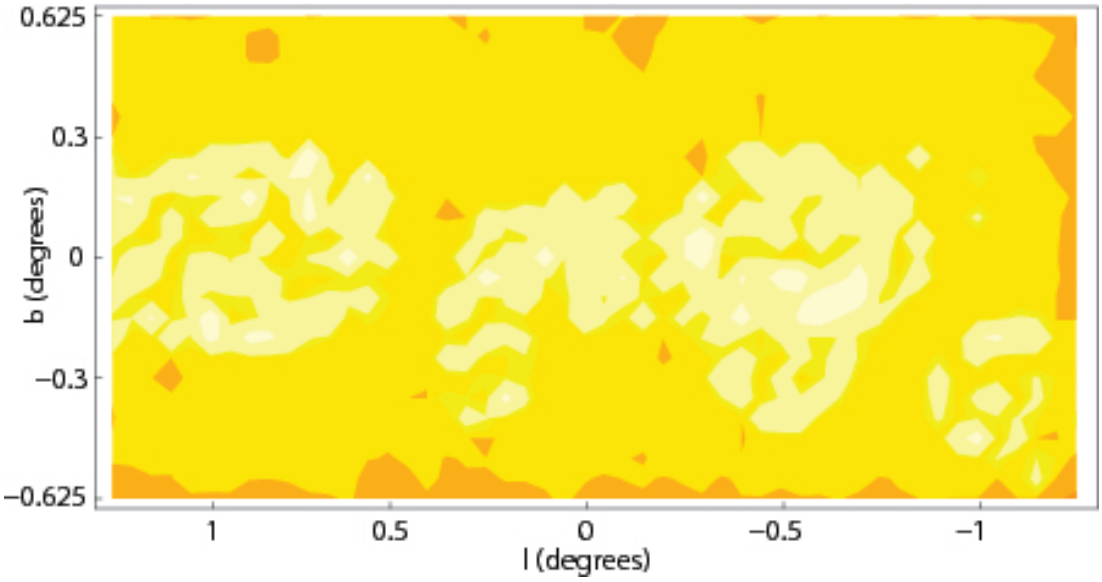

(a)

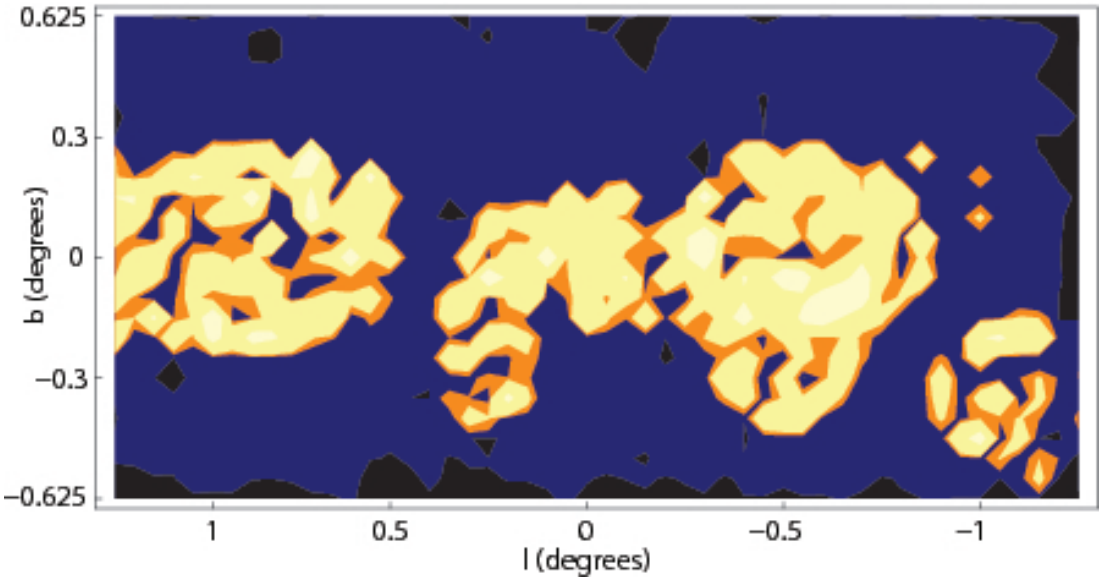

(b)

Figure 3.10: (a–b) — γ-ray emission map for a scenario in which the protons are accelerated throughout the intercloud medium via e.g. a second-order Fermi process. The average magnetic field strength is 10μG. A plot of the full range of γ-ray counts is fairly uniform (top) and the molecular clouds are highlighted quite well when only the most intense emission is considered (bottom).

stars located near the Galactic Center) breaking apart in collisions with the ambient medium and then subsequently accelerated to high energies by a second-order Fermi process. If this picture is correct, we may be able to reduce the highlighting of the point sources in our simulations since the heavier nuclei will propagate away from their origin before disintegrating and producing protons. These protons will travel even further as they reflect off magnetic mirrors and gain sufficient energy to be considered cosmic rays.

Also, though we considered only the TeV γ-ray emission in our calculations, the particle cascade results in longer wavelength radiation, too. For example, the leptons created from a *pp*-scattering event ought to produce synchrotron emission as they are accelerated by the magnetic field. These lepton radio maps, in conjunction with the TeV γ-ray maps, can provide valuable insight into the possible environmental conditions at the Galactic center.

4. The Asymmetric Positron Distribution in the Galactic Disk

4.1. Introduction

Electron-positron annihilation is signified by gamma-ray line emission at 511keV. Since its first detection from the inner regions of the Galaxy in 1972 (Johnson, Harnden, & Haymes) and later confirmation in 1978 (Leventhal, MacCallum, & Stang), the origin of the anti-particle at the heart of this emission has not been conclusively determined. Suggestions include, but are not limited to, cosmic-ray interactions with the interstellar medium (Ramaty, Stecker, & Misra 1970), the decay of radioactive nuclei produced by supernovae (see e.g. Clayton 1973), and light dark matter annihilation (Rudaz & Stecker 1988; Boehm et al. 2004).

In an attempt to constrain the possible sources, Knödlseder et al. (2005) performed a detailed study of the 511keV line emission morphology. They found no evidence of point-source annihilation radiation. Instead, the emission from the Galactic bulge appears diffuse and symmetric about the Galactic center, with a FWHM extent of $\sim 6^{\circ}$. The measured photon flux from this region is measured to be 1×10^{-3} photons cm^{-2} s^{-1}.

With the increased sensitivity and spatial resolution of the SPI imaging spectrometer aboard INTEGRAL, it is possible to map the much fainter 511keV emission (7×10^{-4} photons cm^{-2} s^{-1}) from the inner Galactic disk. Weidenspointner et al. (2008) find a distinct asymmetry in the disk component, estimating the flux from negative longitudes exceeds that from corresponding positive longitudes by a factor of 1.8 (see Figure 4.1). Since observations indicate that the conditions in the interstellar medium on either side of the Galactic center are more-or-less equal, Weidenspointner et al. propose that the electron-positron annihilation asymmetry is due to an asymmetry in the positron production.

One population of objects that may provide an explanation are hard low-mass X-ray binaries (LMXBs)(Weidenspointner et al. 2008). Unlike soft (<200keV) LMXBs and high-mass X-ray binaries (HMXBs) which are distributed uniformly throughout the inner Galaxy, hard LMXBs at negative longitudes outnumber those at positive longitudes 45 to 26 — a factor of 1.7, similar to the ratio of negative to positive longitude annihilation flux (Bird et al. 2007). Figure 4.2 shows the projected positions of these hard LMXBs onto the plane of the sky.

This apparent correlation between the positions of the LMXBs in the inner regions of the Galaxy and the observed 511keV electron-positron annihilation radiation morphology is intriguing and worthy of further examination. We begin by describing the positron injection energies in Section 4.2 and review the processes and rates at which these positrons will annihilate and cool in Sections 4.3 and 4.4, respectively.

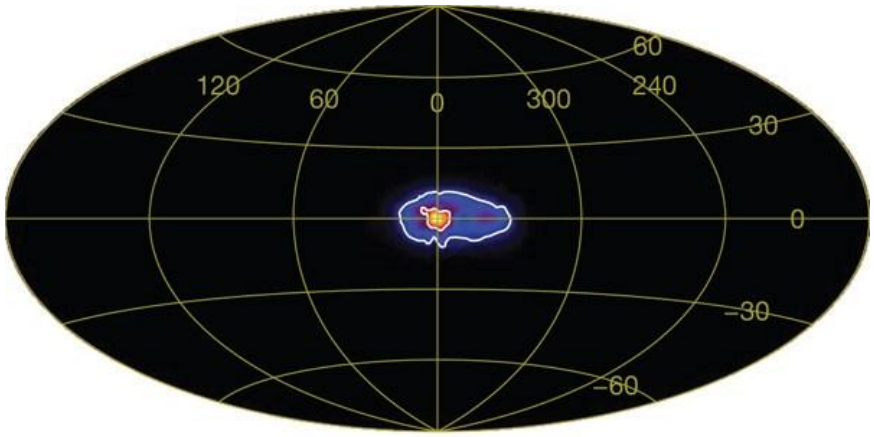

Figure 4.1: Map of the 511keV line emission as measured by INTEGRAL/SPI. The white contour lines correspond to intensities of 10^{-3} and 10^{-2} photons cm^{-2} s^{-1} sr^{-1}. The emission is obviously skewed towards negative longitudes. (Weidenspointner et al. 2008)

The ability of the positrons to diffuse away from their source and fill the interstellar medium is a core issue so we detail the method by which we propagate the positrons in our simulations in Section 4.5. We end with a discussion of the results and the conclusions drawn from them.

4.2. Positron Energies

Though the origin of the positrons remains a mystery, calculations by Beacom, Bell, & Bertone (2004) and Beacom & Yüksel (2006) require positrons to be injected with initial energies of less than $\approx$ 3MeV regardless of the means by which they are produced. The contribution from γ-rays emitted via inflight annihilation and internal bremsstrahlung from positrons with energies greater than this would cause the observed γ-ray flux to exceed that measured by INTEGRAL.

Having an upper limit for the allowed positron energies gives us a means to discriminate between possible production methods. For example, the scenario in which positrons are created in the annihilation of dark matter particles, whose masses usually fall in the range 10GeV - 10TeV, is unfeasible in light of the given energy constraint. Even by restricting the argument to *light* dark matter (1-100MeV), the vast majority of the masses would be disallowed.

The decay of radioactive nuclei produced by explosive nucleosynthesis in supernovae, however, remains a viable method of positron creation. A significant number of positrons is expected from the decay chain ^{44}Ti $\rightarrow ^{44}$Sc $\rightarrow ^{44}$Ca since the relatively long life of ^{44}Ti (89 years) allows nearly all of the positrons (>97%)to survive or es-

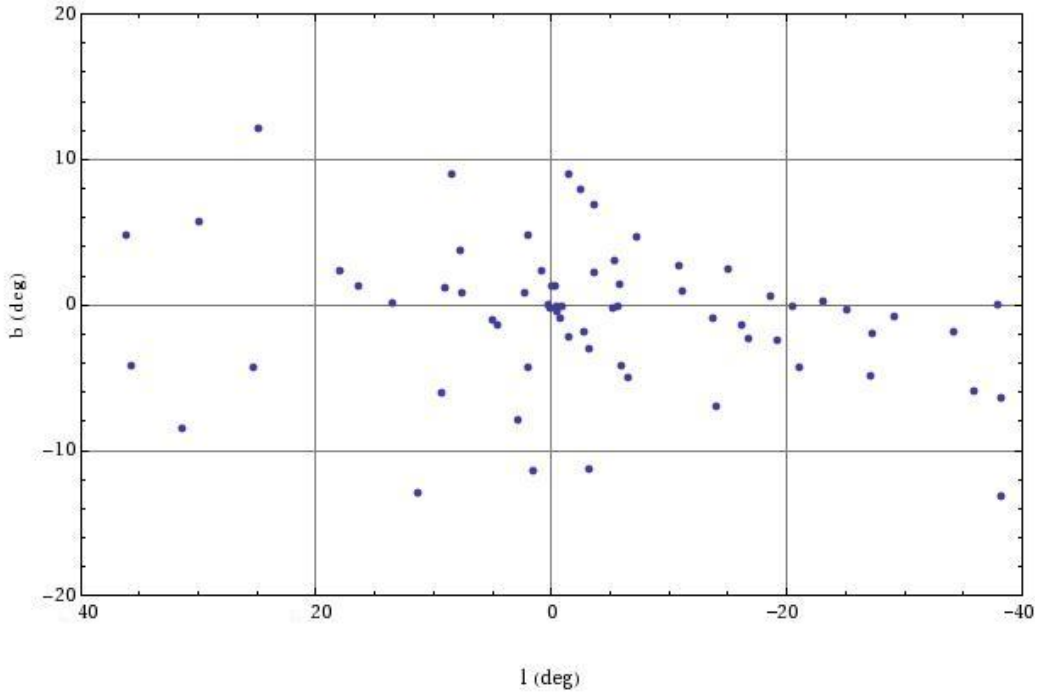

Figure 4.2: Map of the hard LMXBs located in the inner region of the Galaxy, projected onto the plane of the sky. The asymmetric distribution of these objects towards negative longitudes may provide an explanation for the observed 511keV line flux.

cape from the expanding supernova ejecta (Chan & Lingenfelter 1993). The β^+ decay of ^{44}Sc results in positrons with a maximum kinetic energy of ~ 1.5MeV and a mean energy of ~ 0.6MeV. An almost identical positron spectrum occurs in the reaction $^{56}\text{Ni} \rightarrow ^{56}\text{Co} \rightarrow ^{56}\text{Fe}$ though few of the positrons produced in this process escape the ejecta due to the fact that ^{56}Ni has an average lifetime of only 8.8 days (Milne, The, & Leising 1999) and ^{56}Co β^+ decays to ^{56}Fe just 19% of the time. A more direct measurement of the positron contribution from the decay of ^{26}Al can be made. Compared to ^{56}Ni and ^{44}Ti, ^{26}Al is a long-lived isotope with a mean lifetime of $\tau_{26} \sim 1 \times 10^6$ years. When ^{26}Al decays to ^{26}Mg, a 1.809 MeV line photon is emitted and, 82% of the time, a positron is produced. From observations of the 1.809 MeV emission, Diehl et al. (2006) estimate a total ^{26}Al mass of $M_{26} \sim 2.8 \pm 0.8 M_\odot$ thus implying a positron production rate of $\sim 0.82 M_{26}/26 m_p \tau_{26} \sim (0.34 \pm 0.10) \times 10^{43}$ e$^+$s^{-1} (Higdon, Lingenfelter, & Rothschild 2009). This is $\sim 15\% \pm 4\%$ of the total measured positron annihilation rate of $\sim (2.3 \pm 0.2) \times 10^{43}$ e$^+$s^{-1}. The energy spectrum of the positrons created from this decay is softer than that from the decay of ^{44}Ti and ^{56}Ni, with a maximum energy of ~ 1.15MeV and an average energy of ~ 0.45MeV.

The model under consideration in this work, that the positrons are from LMXBs, also satisfies the Beasom & Yüksel (2006) energy constraint. An estimated $\sim 10^{41}$ $e^{+}s^{-1}$ are created by $\gamma + \gamma \rightarrow e^{+} + e^{-}$ interactions in the hot inner regions of the compact object's accretion disk (see e.g. Misra & Melia 1993). These electron-positron pairs can cool to 1-10keV and then be blown away from their source by soft radiation, thereby creating a semi-relativistic wind, as suggested by Beloborodov (1999). Alternatively, the pairs might be injected into the interstellar medium by jets, the presence of which is inferred from radio emission believed to be due to synchrotron radiation. Jet speeds range from 0.1–0.9c, where c is the speed of light, giving rise to positrons with energies 2.5-660keV, well below the 3MeV limit.

4.3. Annihilation Rates

Though the physical conditions surrounding each LMXB positron source will undoubtedly vary, we will assume a simplified situation in which all sources are embedded in the same uniform, homogeneous medium. The interstellar gas is chosen to be in the warm ($T = 10^5$K) ionized phase with average hydrogen density $n_H = 0.5\text{cm}^{-3}$, average helium density $n_{He} = 0.5\text{cm}^{-3}$, and free electron density $n_e = 6\text{cm}^{-3}$.

The three main mechanisms by which positrons moving through the interstellar medium can annihilate are direct annihilation, radiative capture, and charge exchange. In a direct annihilation, a positron annihilates with a free electron without first forming positronium producing two 511 keV photons in the process. If the ambient electrons obey a Maxwell-Boltzmann distribution $f_{mb}(E_{-})$, then the rate at which positrons of energy E_{+} will annihilate is given by

$$R_{da}(E_{+}) = cn_e \int f_{mb}(E_{-})dE_{-} \int_{-1}^{1} f_{kin}(E_{+}, E_{-})\sigma_{da}(E_{+}, E_{-})\frac{d\mu}{2} \tag{4.1}$$

where

$$f_{kin} = [\beta_{-}^2 + \beta_{+}^2 - \beta_{-}^2\beta_{+}^2(1-\mu^2) - 2\beta_{-}\beta_{+}\mu]^{1/2} \tag{4.2}$$

takes into account the kinematics of two-particle motion and

$$\beta_{\pm} = \left[\frac{2E_{\pm}m_ec^2 + E_{\pm}^2}{(E_{\pm} + m_ec^2)^2}\right]^{1/2} \tag{4.3}$$

is the usual expression for the positron/electron speed in terms of the speed of light c. The cross-section for this process is obtained from the plane-wave approximation

$$\begin{aligned}\sigma_{da} = {} & 2\pi\left(\frac{\alpha}{\beta}\right)(1 - e^{-2\pi\alpha/\beta})^{-1}\left(\frac{\pi r_0^2}{\gamma+1}\right) \\ & \times \left[\frac{\gamma^2+4\gamma+1}{\gamma^2-1}\ln(\gamma + (\gamma^2-1)^{1/2}) - \frac{\gamma+3}{(\gamma^2-1)^{1/2}}\right]\end{aligned} \tag{4.4}$$

where

$$\beta = \left[\frac{(1-\beta_+\beta_-\mu)^2 - (1-\beta_+^2)(1-\beta_-^2)}{(1-\beta_+\beta_-\mu)^2}\right]^{1/2} \tag{4.5}$$

is the relative speed (in units of c) between the elctrons and positrons and $\gamma = (1 - \beta^2)^{-1/2}$ is the relative Lorentz factor.

In a radiative capture event, the positron and free electron annihilate after first forming positronium. There is a 25% probability that the positronium will be in the singlet spin zero state in which case two 511keV photons will result. Otherwise, annihilation from the triplet spin 1 state will produce three continuum photons. The capture rate is given by

$$R_{rc}(E_+) = \sum_i cn_e \int f_{mb}(E_-)dE_- \int_{-1}^{1} f_{kin}(E_+, E_-)\sigma_{rc}(E_+, E_-)\frac{d\mu}{2} \tag{4.6}$$

whre the sum accounts for the possibility that the positronium can be formed in an excited state. The cross-section for capture into the i-th state is given by

$$\sigma_{rc} = \frac{2^4}{3^{3/2}}\frac{he^2}{m^2c^3}\frac{\chi^2}{(E+\chi/i^2)E}\frac{g}{i^3} \tag{4.7}$$

whre m is the reduced mass, $\chi = 6.8$eV is the positronium ionization energy from the ground state, and g is the Gaunt factor, set to unity for simplicity.

Charge exchange occurs when a positron forms positronium with the electron from a singly-ionized helium atom thereby completely ionizing the helium ($e^+ + \mathrm{He}_{II} \rightarrow \mathrm{Ps} + \mathrm{He}_{III}$). The rate at which this interaction occurs is given by

$$R_{ce}(E_+) = n_{HeII}\beta_+ c\sigma_{ce}(E_+) \tag{4.8}$$

For the cross section, we use

$$\sigma_{ce}(E_+) = 2.4 \times 10^{-16}\mathrm{cm}^2 \left(\frac{E_+}{E_1} - 1\right)\exp(1 - E_+/E_1) \tag{4.9}$$

This is an empirical expression based on measurements of the cross sections for the reactions $e^+ + \mathrm{H}_I \rightarrow \mathrm{Ps} + \mathrm{H}_{II}$ (Sperber et al. 1992) and $e^+ + \mathrm{He}_I \rightarrow \mathrm{Ps} + \mathrm{He}_{II}$ (Overton et al. 1993) and assuming an energy profile similar to that of the $e^+ + \mathrm{He}_I \rightarrow \mathrm{Ps} + \mathrm{He}_{II}$ process.

4.4. Cooling Rates

As the positrons propagate, interactions with the environment will cause them to lose energy.

Being accelerated by the magnetic field will cause positrons moving at Lorentz factor $\gamma_+ = (1 - \beta_+^2)^{-1/2}$ to cool via synchrotron radiation at a rate

$$\frac{dE_S}{dt} = -\frac{4}{3}\frac{\sigma_T c}{8\pi}\beta_+^2\gamma_+^2 B^2 \tag{4.10}$$

where σ_T is the Thomson cross-section.

The LMXBs are mostly confined to the region $|l| \leq 30^\circ$ and $|b| \leq 10^\circ$. The starlight in this region has an average ultraviolet energy density $u_{uv} \sim 0.01\text{eV/cm}^3$ (Gondhalekar et al. 1980) and an average infrared energy density $u_{ir} \sim 1\text{eV/cm}^3$ (Porter & Strong 2005). By assuming a blackbody spectrum for these radiation fields, we can assign temperatures of $T_{uv} = 30{,}000\text{K}$ and $T_{ir} = 100\text{K}$. Inverse Compton scattering off these UV and IR photons will cause positrons to lose energy at a rate

$$\frac{dE_\gamma}{dt} = -\frac{4}{3}m_e c^3 \beta_+^2 \gamma_+^2 \left[\frac{u_{uv}\sigma_T}{m_e c^2 + \gamma_+ kT_{uv}} + \frac{u_{ir}\sigma_T}{m_e c^2 + \gamma_+ kT_{ir}}\right] \tag{4.11}$$

The cooling rate due to bremsstrahlung emission is

$$\frac{dE_B}{dt} = -4\alpha r_0^2 m_e c^3 (2n_H + 6n_{He}) \ln(2\gamma_+ - 1/3)\gamma_+ \tag{4.12}$$

where α is the fine structure constant and r_0 is the classical electron radius.

Scattering off a Maxwell-Boltzmann distribution of ambient electrons results in an energy-loss rate

$$\frac{dE_C}{dt} = -m_e c^3 n_e \int f_{mb}(E_-)dE_- \int_{-1}^{1} f_{kin} < \sigma\Delta\gamma > \frac{d\mu}{2} \tag{4.13}$$

where

$$< \sigma\Delta\gamma > = \frac{3\sigma_T(\gamma_- - \gamma_+)}{64\epsilon^2}\left[(4\ln\Lambda + 4\ln 2)\left(\frac{\epsilon^2 + p^2}{p^2}\right)^2 - 2\left(\frac{8\epsilon^4 - 1}{p^2\epsilon^2}\right) + \frac{12\epsilon^4 + 1}{\epsilon^4} - \frac{8p^2}{3}\frac{(\epsilon^2 + p^2)}{\epsilon^4} + \frac{2p^4}{\epsilon^4}\right] \tag{4.14}$$

and the parameters ϵ and p are defined as $\epsilon^2 = (1 + \gamma)/2$ and $p^2 = \epsilon^2 - 1$. Of the four cooling processes mentioned, only this Coulomb interaction had a temperature dependence. Once the positrons have thermalized ($E_+ \sim kT$), this scattering process should not significantly affect the positrons' energy.

4.5. Propagation

In order to simulate the propagation of a significant number of positrons in a reasonable amount of computing time, we employ a similar mixed exact/statistical approach as was used in Chapter 3.5. First, we perform a short simulation in which we

solve for the exact trajectories of $\sim$ 5000 positrons using the Lorentz force equation, $\mathbf{F} = q\mathbf{v} \times \mathbf{B}$. The magnetic field is generated as described in Chapter 2. For this research project, we use three different magnetic field configurations: a completely turbulent field, a total field with an equal mix of turbulent and ordered magnetic energy densities ($\eta = 2$), and a weakly turbulent field ($\eta = 0.22$).

The magnetic field inertial range extends over a length scale of $\lambda_{min} = 2 \times 10^5$ meters to $\lambda_{max} = 2 \times 10^{17}$ meters, equivalent to a wavenumber scale from $k_{min} = 2\pi/\lambda_{max}$ to $k_{max} = 2\pi/\lambda_{min}$. To carry out the sum in Equation 2.3, we use 200 wavevectors evenly distributed between k_{min} and k_{max} on a logarithmic scale. The inner scale, λ_{min} is based on astronomical radio observations of interstellar scattering (ISS) by Spangler & Gwinn (1990) who found a value between 60-200km to be consistent with the data. This result was later confirmed and slightly refined to λ_{min} =300km by Molnar et al. (1995) using high quality Very Long Baseline Interferometry (VLBI) data. The remarkable span of the inertial range (12 orders of magnitude) is demonstrated in the composite plot of Armstrong, Rickett, and Spangler (1995; Figure 1 of their paper). More recently, Rickett et al. (2009) determined an inner scale of 70-100km and an outer scale of 1-20pc based on studies of the decaying shape of pulses broadened by ISS from pulsar PSR J1644-4559.

When solving the equation of motion, we use a Runge-Kutta scheme and take timesteps of $\Delta t = f\tau_{gyr}$ where τ_{gyr} is the gyroperiod and f is a random number between 0 and 1 which is re-assigned after each advancement. We find that this produces similar results as taking time-steps limited by the size of the smallest magnetic field fluctuations, $\Delta t = \lambda_{min}/v$, but is computationally much quicker. The particles are followed for a total time of $t_{max} = 10^6$ seconds - this allows the particles to sample a decent range of magnetic turbulence length scales yet is still small compared to the total lifetime of positrons in this environment which we find to be on the order of 10^{12} seconds. At the end of the short simulation, the position and velocity vectors of each positron are recorded.

The final spatial distribution depends not only on the initial energy, but also on the initial injection angle relative to the uniform magnetic field component (e.g. very energetic particles that emerge from a point source nearly parallel to the uniform magnetic field will be expected to travel much further than low-energy counterparts injected perpendicular to the field). With this in mind, we considered five different initial energies (E_+ = 0.1MeV, 0.5MeV, 1MeV, 2MeV, and 3MeV) and, for each energy, collected data for three separate scenarios corresponding to initial injection angles $0 \leq \theta_{v,i} \leq 30°$, $30° \leq \theta_{v,i} \leq 60°$, and $60° \leq \theta_{v,i} \leq 90°$ where $\theta_{v,i}$ is the angle between the initial velocity vector and the uniform magnetic field.

The data from the short simulations allow us to create the particle statistics we will need to run full-length simulations. We tabulate the distribution of particles as a function of net distance traveled (r) and final angle relative to the uniform magnetic field for both the position (θ_r) and velocity (θ_v) vectors. To characterize the net

distance traveled, we first determine the minimum and maximum net distance any particle has covered and then divide this interval into ten bins. The fraction of the total number of particles falling into each bin is tabulated. Similarly for both θ_r and θ_v, the fraction of particles in the interval $(\theta_i, \theta_i + \Delta\theta)$ is tallied where $\theta_{min} = 0$, $\theta_{max} = 180°$, and there are ten bins of size $\Delta\theta = 180°/10$. Figures 4.3, 4.4, and 4.5 show the data points and corresponding fits for positrons injected with energy 3MeV into an $\eta = 2$ magnetic field. The fits are polynomial functions, with leading order between zero and seven, whose coefficients are determined through χ^2 minimization. Similar fits were made for the other energies and for each magnetic field configuration.

We then apply the following Monte-Carlo technique to these probability distributions to advance the particles in 10^6 second increments. At each timestep, three distinct random numbers (x_1, x_2, and x_3) are generated representing a portion of the normalized area under each of the three probability curves (N vs r, N vs θ_r, and N vs θ_v). The new position and orientation relative to the ordered field are those values of r, θ_r, and θ_v with areas x_1, x_2, and x_3 to their left, respectively.

For example, if a 3MeV positron's velocity vector makes an angle of 70° with respect to the uniform field, then we would use the probability distributions given in Figure 4.5 since these represent the distribution data for particles with velocity vectors in the interval $60° \leq \theta_v \leq 90°$. Now, if the generated random number set is $(x_1, x_2, x_3) = (0.20,\ 0.84,\ 0.38)$, then we have the situation presented in Figure 4.6. The net distance traveled by the positron would be $r = 5.527 \times 10^{10}$m since this is the value of r with an area of 0.20 to its left. The particle's new position coordinates would be $(x_{new}, y_{new}, z_{new}) = (x_{old} + r\sin\theta_r\cos\phi, y_{old} + r\sin\theta_r\sin\phi, z_{old} + r\cos\theta_r)$ where $\theta_r = 138.03°$, which is the value of θ_r with a normalized area of 0.84 to its left, and ϕ is the azimuthal angle randomly chosen such that $0 \leq \phi \leq 360°$. The angle between the new velocity vector and the uniform magnetic field is $\theta_v = 39.25°$, which is the angle with an area of 0.38 to its left, so, in the next timestep, we would use the probability distributions given in Figure 4.4 because these represent the distribution data for particles with velocity vectors oriented with $30° \leq \theta_v \leq 60°$.

The energy losses mentioned in Section 4.4 are calculated at each step until the positrons thermalize, $E_+ \sim kT$, at which point it is assumed that no net energy changes occur. Likewise, the fraction of the positron population lost to annihilation is determined according to the discussion in Section 4.3. The simulation ends when only 1% of the original positrons remain.

By using these fits - interpolating between energies as needed - together with the given cooling and annihilation rates, we were able to quickly and accurately model the propagation of $\sim 10^5$ positrons injected into the interstellar medium by a single point source.

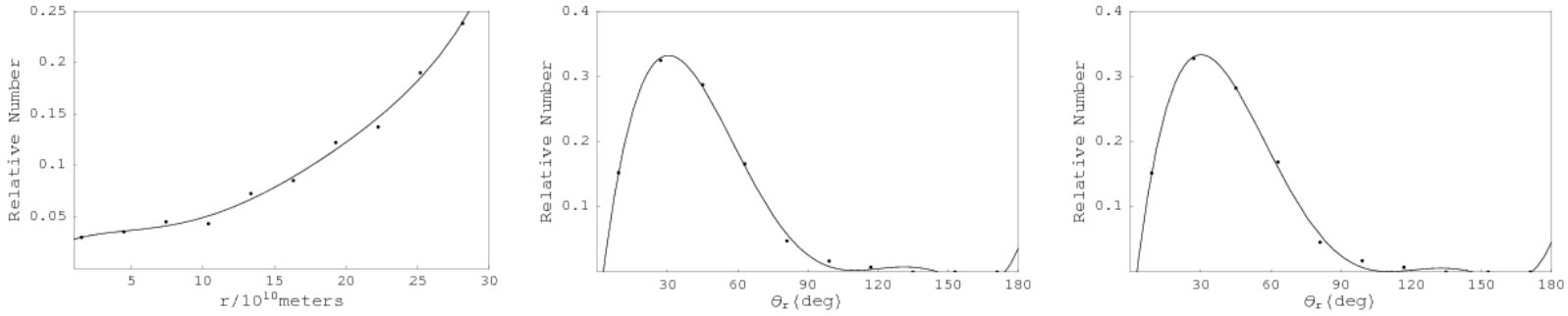

Figure 4.3: (a–c) — These plots are a sample of the statistics used to propagate particles as described in Section 4.5. The graphs show the distribution of the relative number of positrons as a function of a.) net distance traveled r, b.) position angle relative to the mean magnetic field θ_r, and c.) velocity angle relative to the mean field θ_v when the initial velocity vector $\theta_{v,i}$ makes an angle $0° \leq \theta_{v,i} \leq 30°$ relative to the mean field. The particles were injected with an initial energy of 3MeV and followed for 1000s through a magnetic field in which the turbulent and ordered components contribute equally to the total energy density.

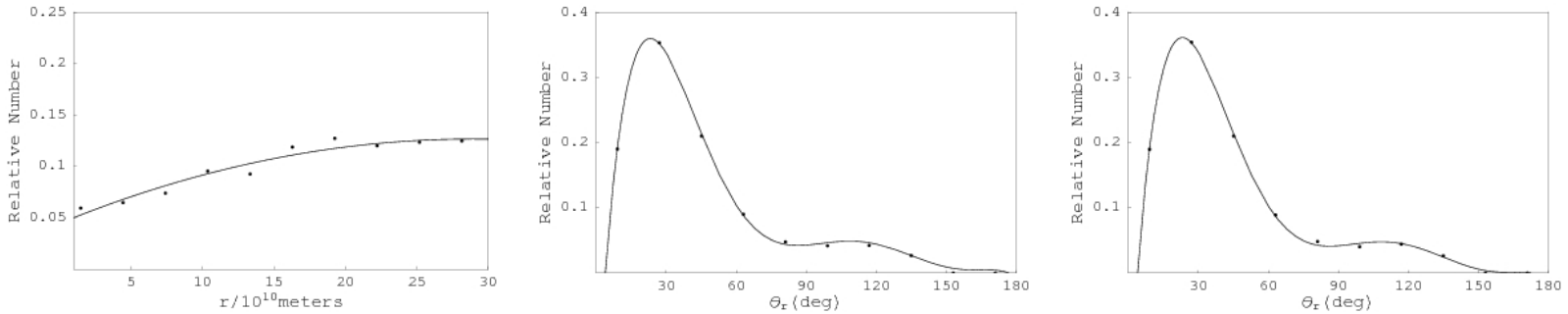

(a) (b) (c)

Figure 4.4: (a–c) — Same as Figure 4.3 except here the initial velocity vector makes an angle $30° \leq \theta_{v,i} \leq 60°$ relative to the mean field.

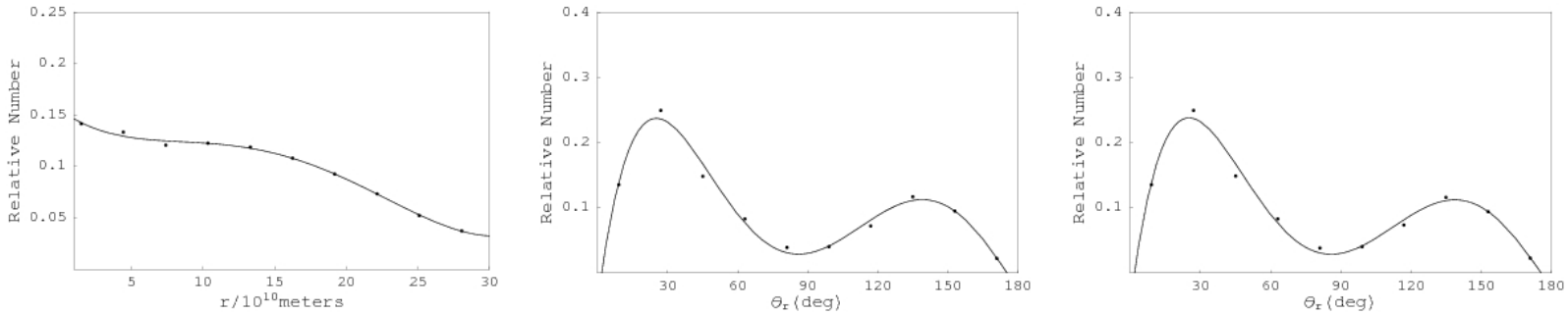

(a) (b) (c)

Figure 4.5: (a–c) — Same as Figures 4.3 and 4.4 except here the initial velocity makes an angle $60° \leq \theta_{v,i} \leq 90°$ relative to the mean field.

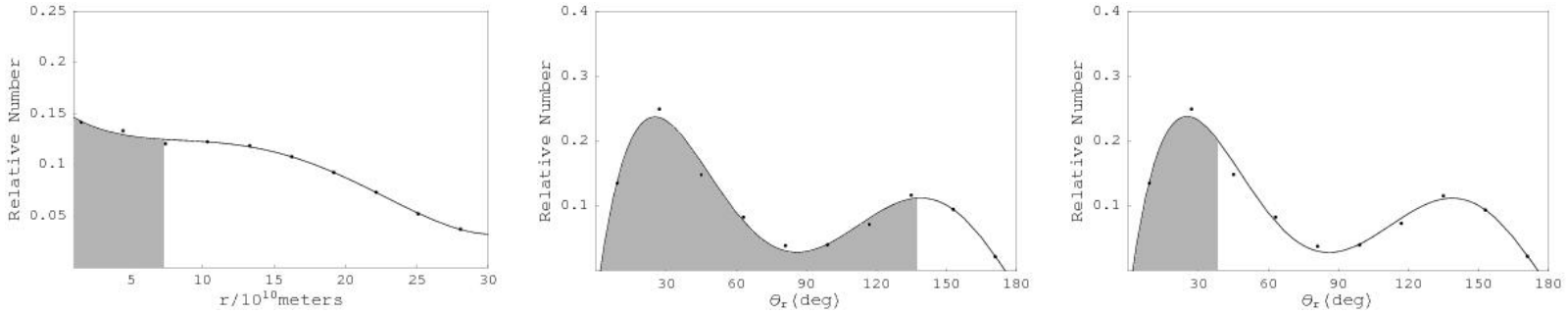

(a) (b) (c)

Figure 4.6: (a–c) — Method for propagating positrons based on statistics. Given the random variable set (x_1, x_2, x_3) = (0.20, 0.84, 0.38), the following parameters (r, θ_r, θ_v) = (5.527×10^{10}m, 138.03°, 39.25°) will be used to calculate the new position and velocity of the positron since these are the values of r, θ_r, and θ_v with normalized areas of 0.20, 0.84, and 0.38 to their left, respectively.

4.6. Results and Discussion

The main goal of this study is to determine whether hard LMXBs can be the source of the positrons in the inner Galactic disk. However, how well the positrons can propagate and fill the space between LMXBs is a key factor in making this determination. Since it is possible that the structure of the insterstellar magnetic field plays a major role in the positron spatial distribution, we consider three different (Kolmogorov spectrum) field configurations — completely turbulent (no ordered component), an equal mix of order and turbulence, and highly ordered (little turbulence) — constructed as described in Chapter 2 and by setting the value of η appropriately in Equations 2.6 and 2.7 ($\eta = 2$ for equally turbulent/ordered field and $\eta = 0.22$ in the highly ordered case, corresponding to a field in which 90% of the total energy density comes from the ordered component).

Figure 4.7 shows projected maps of the 511keV line emission produced by a point source located at the origin with a continuous injection of 3MeV positrons for each of the three magnetic field configurations. As would be expected, a completely turbulent magnetic field produces an emission pattern with no directional preference (Figure 4.7a). The γ-ray distribution is symmetric about the origin and extends no more than $\sim$0.4pc in radius. The presence of a tangled magnetic field has a huge impact on the positron propagation distance as free-streaming positrons are estimated to travel hundreds, if not thousands, of parsecs before annihilating. If the magnetic field surrounding a LMXB system is fully turbulent, the positrons will effectively remain trapped at their source and not escape into the interstellar medium.

The γ-ray emission produced by a positron source embedded in a magnetic field in which the turbulent, $\delta\mathbf{B}$, and ordered, $\mathbf{B}_0$, components equally contribute to the total energy density is shown in Figure 4.7b. Here, $\mathbf{B}_0$ lies parallel to the x-axis. The positron distribution is clearly extended horizontally, along the direction of the large-scale ordered field. As the positrons spiral around the magnetic field lines, their pitch angle relative to the mean field is perturbed by the turbulent fluctuations giving the projected 511keV map an elliptical shape. The semi-major axis extends to $\sim$1pc which is almost three times farther than the emission spread in the case of a completely turbulent field.

Figure 4.7c is a plot of the emission pattern for the scenario in which the magnetic field has only a very weak turbulent component. Again, just as in Figure 4.7b, the mean field points along the x-axis. The positron population is strongly aligned with the ordered field, showing relatively little scatter perpendicular to the field compared to the previous case. Since the particles are more constrained to move along the field lines, they necessarily reach greater distances than those in completely turbulent or half ordered/half turbulent fields. The emission spans $\sim$10pc along the field but is only $\sim$2pc in width.

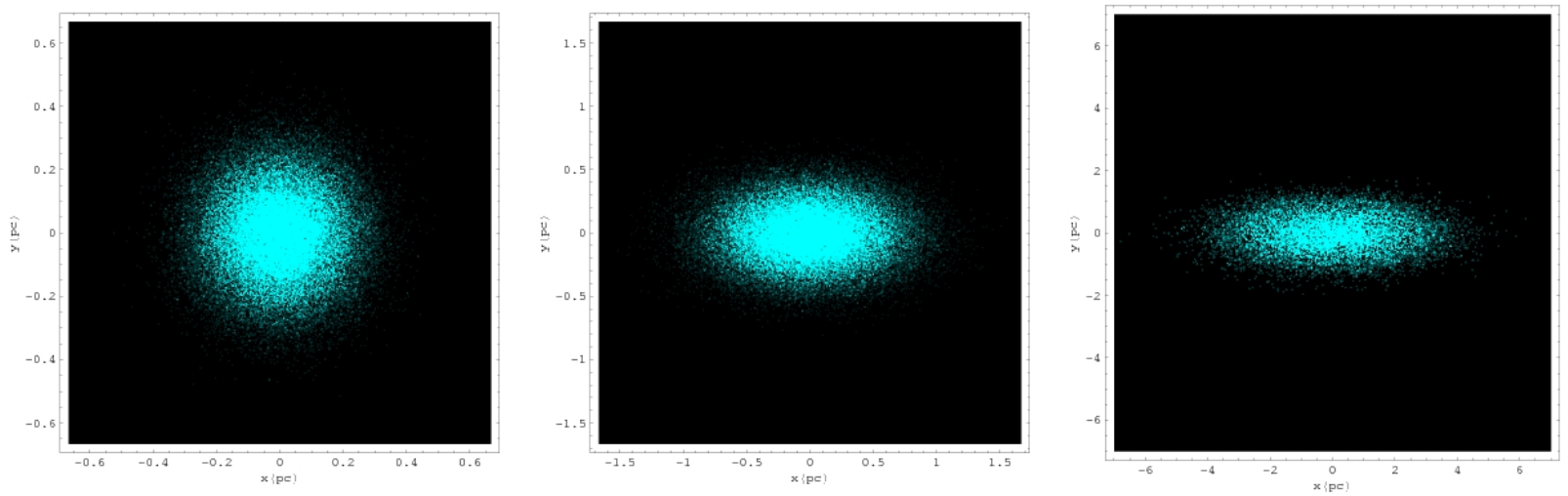

(a) (b) (c)

Figure 4.7: (a–c) — Projected emission plots of the template solutions for the 3 different magnetic field configurations: a.) a completely turbulent field, b.) a half turbulent/half ordered field, and c.) a highly ordered (e.g. weakly turbulent) field. Note that each image is plotted on a different length scale.

Because we have made the simplifying assumption that the environment around each LMXB is the same, the data used to create the electron-positron line emission plots in Figure 4.7 can be used as a template solution that can be overlaid at each LMXB position providing us with a complete picture of the Galactic disk emission. In order to properly take perspective into account (sources closer to us should take up a larger angle in our field-of-view), a line-of-sight position is first randomly assigned to each LMXB, the template data are copied at each source location, and then a contour plot of the disk emission projected onto the plane of the sky is made. A smoothing routine is applied to the raw plots to emulate the 2.6° FWHM point-spread function of the SPI detector. The final, smoothed 511keV disk emission plots are presented in Figures 4.8, 4.9, and 4.10.

Upon inspection, two features are immediately obvious. First, there is virtually no difference in the γ-ray emission patterns for the three magnetic field configurations. This is not entirely unexpected as the distance the positrons are able to travel before annihilating only ranges from 0.3pc in the completely turbulent case to 5pc in the strongly ordered case — much too small of a difference to be distinguishable by SPI. Second, although the point-like nature of some of the sources becomes obscured, the simulated emission appears clumpy compared to the relatively smooth 511keV distribution observed by INTEGRAL (Figure 4.1). Again, this can be attributed to the positrons' inability to propage a significant distance away from their point of origin.

There are, however, features common to both the simulated and physically observed emission patterns. The 10^{-2} photons cm^{-2} s^{-1} sr^{-1} contour line in Figure 4.1 is slightly heart-shaped with a protuberance on the left lobe. A similar shape, of roughly the same size and position, appears in Figures 4.8, 4.9, and 4.10. Although patchy, these figures also indicate γ-ray counts biased towards negative longitudes as required by INTEGRAL. The calculations performed did not account for any possible large-scale, bulk transport of positrons due to e.g. a galactic wind. The study of galactic winds is still in its early stages, but observations indicate speeds of hundreds of km s^{-1} are possible. Veilleux, Cecil, & Bland-Hawthorn (2005) give a detailed review of the theory of galactic winds. It is not entirely unfeasible that the addition of a galactic wind may sufficiently blur the point-source emission farther from the Galactic center, creating the diffuse emission seen by SPI.

4.7. Conclusion

To summarize, we have run Monte-Carlo simulations of the propagation of positrons through three different magnetic field configurations (completely turbulent, equally turbulent/ordered, and highly ordered) to determine whether hard low-mass X-ray binaries (LMXBs) could be the source of the positrons responsible for the diffuse 511keV γ-ray line emission coming from the inner Galactic disk. By overlaying a template solution at each LMXB system position, a complete picture of the disk

emission is produced. Though some of the features of the observed e^+/e^- annihilation radiation are reproduced in the simulations, the positrons are not able to adequately fill the interstellar medium by diffusing through the magnetic field turbulence for any of the magnetic field scenarios considered here. An additional, bulk-transport mechanism (such as a galactic wind or the presence of jets from the compact star in the LMXB system) could possibly carry the positrons far enough from their origination point to produce the smooth emission observed by the INTEGRAL satellite.

LMXBs were proposed as the possible source for positron production because their asymmetric distribution through the inner Galaxy is similar to the measured asymmetry in 511keV photon flux. However, as mentioned in Section 4.2, of the many proposed positron-producing candidates, supernovae remain at the top of the list (see e.g. Clayton 1973; Ramaty & Lingenfelter 1979; Knödlseder et al. 2005; Guessoum et al. 2006). In the supernovae situation, the problem lies not so much in producing a sufficient number of positrons, but in having a sufficient number of positrons survive and escape from the ejecta into the interstellar medium. Colgate, Petschek, & Kriese (1980) realized the importance of positron escape in their attempt to explain the light curve of Type I supernovae. Under the conclusion that many supernovae are produced in stars with strong magnetic fields, they determined that positrons produced in the decay chain $Ni^{56} \rightarrow Co^{56} \rightarrow Fe^{56}$ would remain trapped in the nebula due to a dynamo-produced toroidal magnetic field and therefore would be incapable of contributing to the either the peak luminosity or width of the optical peak. To remedy this, a "combed" radial magnetic field was assumed, produced in a star with an initially dipole field when an outer small mass fraction expands nearly relativistically ahead of the escaping positrons.

Chan & Lingenfelter (1993) carried out a detailed calculation of the positron survival fraction from different types of supernovae. Additionally, considering that the radioactive Ni^{56} is usually buried in the deeper layers of the supernova ejecta, the effect of "mixing", a situation in which dynamic instabilities carry Ni to the outer ejecta layers, on positron survival rates was also included. These supernovae models, mixed and unmixed, were tested under two extreme magnetic field configurations: a small-scale turbulent field where positrons are locally trapped at their production site and a large-scale radially-combed field where positrons stream freely along field lines. Chan & Lingenfelter conclude that the decay chains $Ni^{56} \rightarrow Co^{56} \rightarrow Fe^{56}$, $Ti^{44} \rightarrow Sc^{44} \rightarrow Ca^{44}$, and $Al^{26} \rightarrow Mg^{26}$ produce enough surviving positrons to account for the observed annihilation radiation.

One of the issues with the supernovae scenario is that the ratio of the e^+/e^- line emission from the Galactic bulge to the Galactic disk is $\sim$1.4 while the supernovae bulge-to-disk ratio is only $\sim$0.33, roughly a factor of 4 too small. Higdon, Lingenfelter, & Rothschild (2009) explain this discrepancy as due to the differential propagation of positrons through the various phases of the interstellar medium. They deduce that positrons originating in the bulge are produced in the very hot plasma phase where

they have little chance of cooling to the necessary temperature before annihilating. Instead, the vast majority (∼80%) are expected to reach either the warm ionized envelopes of the inner bulge (R < 0.5kpc) molecular clouds where they thermally annihilate leading to narrow (∼1.2keV) 511keV line emission or the cool neutral envelopes of the middle bulge (0.5kpc < R < 1.5kpc) molecular clouds where they annihilate in-flight resulting in broad (∼5.8keV) line emission. This accounts for the observed broad/narrow 511keV line ratio of ∼0.5. Meanwhile, positrons originating in the disk have equal probabilities of being produced in either the warm neutral hydrogen phase or in hot superbubbles which can extend out into the Galactic halo. Roughly half escape into the halo leaving the rest to annihilate in the disk. The greater probability for disk positrons to escape results in the larger observed 511keV line flux from the bulge. Not only that, the asymmetry of the inner disk emission is attributed to the asymmetry of the Milky Way's inner spiral arms as viewed from our solar perspective assuming that positrons propagate to and annihilate in the ionized gas of the nearest spiral arm.

Using detailed information about the various phases of the interstellar medium, the production and survival rates of positrons from supernovae, and the distribution and occurrence rates of Galactic supernovae together with a few approximations of positron propagation, Higdon, Lingenfelter, & Rothschild seem to be able to explain all of the features of the observed diffuse e^+/e^- annihilation radiation. One of their key assumptions, though, is that the tubulent MHD cascades do not extend to length scales smaller than the ion-neutral collision mean free path, basically quenched by ion-neutral damping, thus allowing positrons to stream freely along magnetic flux tubes. However, the issue of ion-neutral damping is far from settled and remains an active area of research. Spangler (2007) tackled the issue of the apparent contradiction between the expected distance MHD turbulence could travel in the Diffuse Ionized Gas before dissipating due to ion-neutral collisions (calculated to be $\lesssim$1pc) and the distance it would need to travel to fill the interstellar medium between the supposed turbulence-generators, supernova remnants and star formation regions, which are separated by thousands of parsecs. Two solutions are proposed. First, the calculation of the dissipation length may be correct in which case the turbulence cannot be due to isolated sources but is instead generated locally throughout the ISM by distributed sources such as localized shear flows. Or, if the turbulence does indeed originate in e.g. supernovae, then the ISM may be filled with a web of nearly 100% ionized "channels" though which the fluctuating waves can propagate unattenuated.

Oishi & MacLow (2006) performed numerical simulations of the effect of ambipolar diffusion (the drift of magnetized, ionized gas through a neutral gas coupled by ion-neutral collisions) on MHD turbulence and found it was not able to suppress the formation of structures smaller than the dissipation scale. Likewise, Cho, Lazarian, & Vishniac (2002), using an incompressible MHD code, found the magnetic field continued to have structure below the expected viscous cut-off scale. A year later,

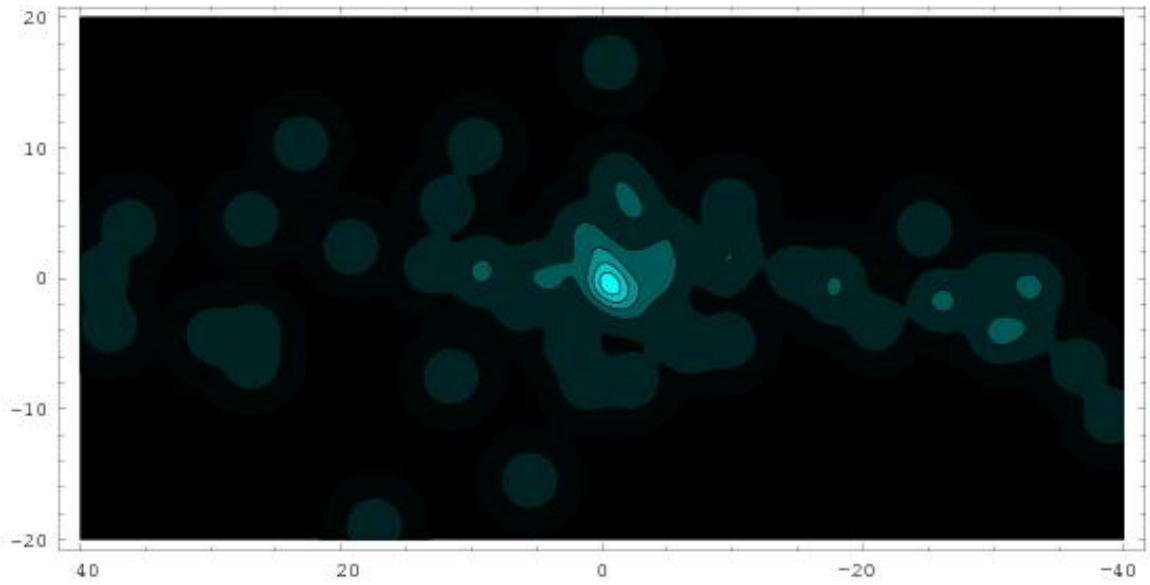

Figure 4.8: Projected and smoothed 511keV emission from LMXB sources embedded in a completely turbulent magnetic field.

Cho & Lazarian (2003) obtained the same result for compressible MHD turbulence, noting that, though viscosity might set the lower scale of hydrodynamic turbulence, on length scales where the viscosity is much greater than the resistivity, magnetic field structures will continue to be created by shear. In discussing the observed spectrum observed in the nearby ISM, Armstrong, Rickett, & Spangler (1995) state "there is no sign of a break or other spectral feature near the collisional scale, at which waves should apparently not exist." They posit that the theoretical work of McIvor (1977) on the role of ion-neutral damping has led some to believe that the critical collisional scale (the point at which the wave frequency ω equals the ion-neutral collision frequency ν_{i-n}) is necessarily the absolute minimum scale on which turbulence can be supported though McIvor's theory shows waves continue to exist even when $\omega \gg \nu_{i-n}$.

Schekochihin & Cowley (2007) have recently published a review on astrophysical MHD turbulence noting that, though much research has been done on the subject, many important questions still remain, to the point that even our basic understanding of the process is incomplete. Until the propagation of positrons, and consequently ISM turbulence, is fully understood, the source of e^+ particles cannot be determined with certainty.

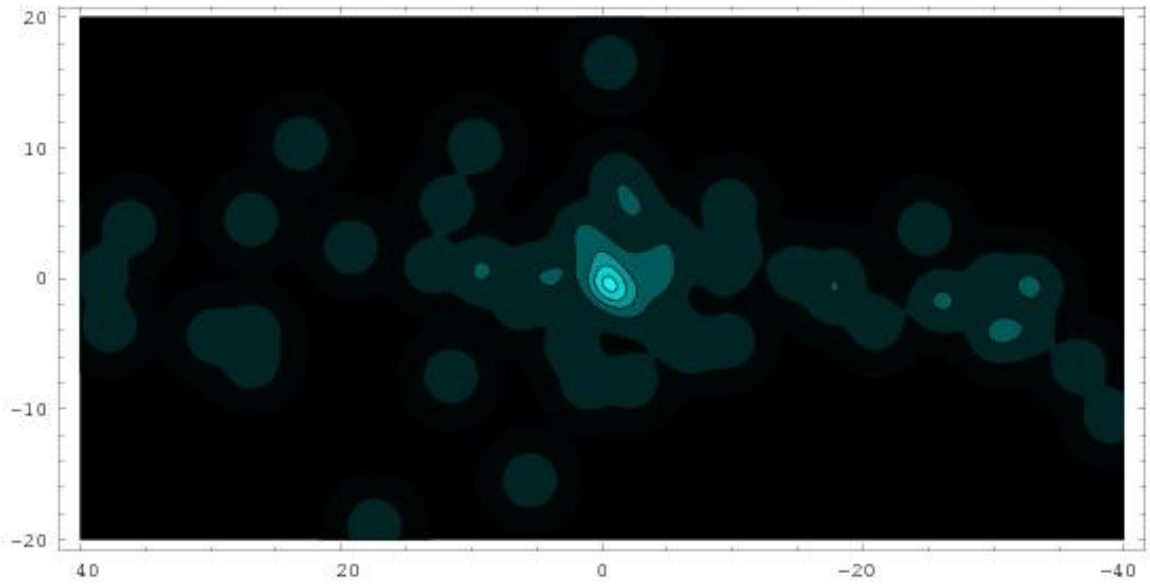

Figure 4.9: Same as Figure 4.8 but for LMXB sources embedded in a half ordered/half turbulent magnetic field.

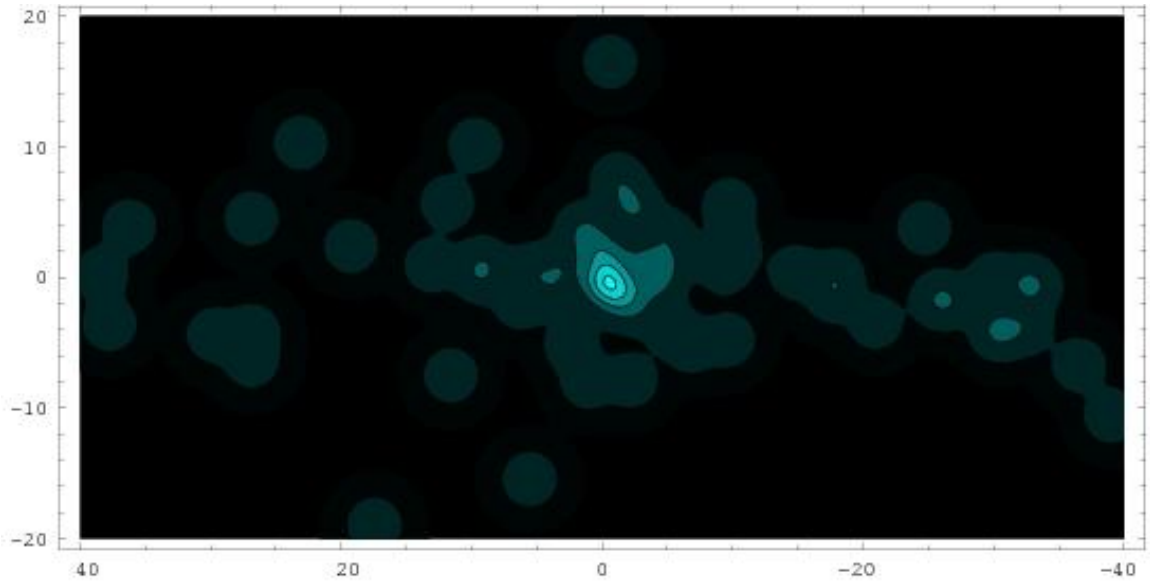

Figure 4.10: Same as the previous two figures but for LMXB sources embedded in a strongly ordered magnetic field.

5. Conclusion

In this work, we have explored the influence of interstellar magnetic field turbulence on the motion of cosmic rays (Chapter 3) and positrons (Chapter 4). Based on these results, we have concluded that the presence of a completely turbulent magnetic field at the Galactic center precludes the possibility that Sagittarius A*, the supermassive black hole at the heart of the Milky Way, is the source of the relativistic protons creating the diffuse γ-ray emission observed by HESS. If there is a small-scale tangled field, the protons must be accelerated throughout the inner 2°, perhaps through second-order Fermi processes, not injected into ISM by point sources . However, if the Non-Thermal Filaments (NSFs) are indicative of a large-scale ordered magnetic field in the region and not just localized enhancements, then it is possible that the additional structured component will allow protons accelerated from a handful of point sources to adequately fill the inner Galaxy.

Simulations testing the theory that hard low mass x-ray binaries (LMXBs) produce the positrons responsible for the diffuse 511keV line flux from the inner Galactic disk do lead to emission patterns with features similar to observations. However, the similarities are not so strong that a positive conclusion can be drawn, certainly not with any conviction. A major issue is the inability for positrons originating from LMXBs located at large longitudes to travel sufficiently far from their source, thus leading to a "clumpy" γ-ray map instead of the smooth, diffuse picture presented by INTEGRAL. The addition of a galactic wind, which would provide a bulk-transport mechanism, may help blur the distinction between point sources. Also, following the lead of Higdon, Lingenfelter, & Rothschild (2009), having the LMXBs farther from the Galactic center occupy a different phase of the ISM than those located nearer the center will make the simulation more realistic.

Of course, much work on the understanding of turbulence, astrophysical or otherwise, remains to be done. Any progress in this subject will necessarily lead to advancements in areas of research which are affected by turbulent motions.

References

[1] Aharonian, F., et al., 2004, A&A, 425, L13

[2] Aharonian, F., et al., 2005, A&A, 432, L25

[3] Aharonian, F., et al., 2006, Nature, 439, 695

[4] Armstrong, J.W., Rickett, B.J., and Spangler, S.R., 1995, ApJ, 443, 209

[5] Bally, J., Stark, A., Wilson, R., Henkel, C., 1985, ApJS, 65, 13

[6] Beacom, J.F., Bell, N.F., and Bertone, G., 2005, Phys. Rev. Letters, 94, 171301

[7] Beacom, J.F. and Yüksel, H., 2006, Phys. Rev. Letters, 97, 071102

[8] Begelman, M., Rudak, B., and Sikora, M., 1990, ApJ, 362, 38

[9] Beloborodov, A.M., 1999, MNRAS, 305, 181

[10] Bhattacharjee, P., 2000, Phys. Rep., 327, 109

[11] Bird, A.J., et al., 2007, Astrophys. J. Supp. Ser., 170, 175

[12] Blasi, P. and Colafrancesco, S., 1999, Astroparticle Phys., 122, 169

[13] Blitz, L., Bloemen, J.B., Hermsen, W., Bania, T.M., 1985, A&A, 143, 267

[14] Boehm, C., et al., 2004, Phys. Rev. Letters, 92, 1301

[15] Champagne, F.H., 1978, J. of Fluid Mech., 86, 67

[16] Chan, K.-W. and Lingenfelter, R.E., 1993, ApJ, 405, 614

[17] Cho, J. and Lazarian, A., 2003, MNRAS, 345, 325

[18] Cho, J., Lazarian, A., and Vishniac, E., 2002, ApJ, 566, L49

[19] Chuss, D., et al., 2003, ApJ, 599, 1116

[20] Clayton, D.D., 1973, Nature Phys. Sci., 244, 137

[21] Colgate, S.A., Petschek, A.G., and Kriese, J.T., 1980, ApJ, 237, L81

[22] Cox, P. and Laureijs, R., 1989, Proc. IAU Symp. 136, 121

[23] Dermer, C.D., 1986, A&A, 157, 223

[24] Diehl, R., et al., 2006, Nature, 439, 45

[25] Fan, C.-Y., 1951, Phys. Rev., 82, 211

[26] Fatuzzo, M. and Melia, F., 2003, ApJ, 596, 1035

[27] Giacalone, J. and Jokipii, J.R., 1994, ApJ, 430, L137

[28] Gondhalekar, P.M., Phillips, A.P., and Wilson, R., 1980, A&A, 85, 272

[29] Grant, H.L., Stewart, R.W., and Moilliet, A., 1962, J. of Fluid Mech., 12, 241

[30] Guessoum, N., Jean, P., and Prantzos, N., 2006, A&A, 457, 753

[31] Güsten, R. and Henkel, C., 1983, A&A, 125, 136

[32] Güsten, R. and Philipp, S., 2004, Springer Proc. Phys., 91, 253

[33] Higdon, J.C., Lingenfelter, R.E., and Rothschild, R.E., 2009, ApJ, 698, 350

[34] Johnson, W.N., Harnden, F.R., and Haymes, R.C., 1972, ApJ, 172, 1

[35] Karol, P.J., 1988, ApJ, 332, 615

[36] Kim, S., Martin, C., Stark, A., Lane, A., 2002, ApJ, 580, 896

[37] Knödlseder, J., et al., 2005, A&A, 441, 513

[38] Kolmogorov, A., 1941, Dokl. Akad. Nauk. SSSR, 30, 301

[39] Leventhal, M., MacCallum, C.J., and Stang, P.D., 1978, ApJ, 225, L11

[40] Markoff, S., Melia, F., and Sarcevic, I., 1997, ApJ, 489, L47

[41] Markoff, S., Melia, F., and Sarcevic, I., 1999, ApJ, 522, 870

[42] Marsch, E. and Tu, C.-Y., 1990, J. of Geophys. Research, 95, 11945

[43] Maurer, J., and Tabeling, P., 1998, Europhysics Letters, 43(1), 29

[44] McIvor, I., 1977, MNRAS, 178, 85

[45] Milne, P.A., The, L.-S., and Leising, M.D., 1999, ApJS, 124, 503

[46] Misra, R. and Melia, F., 1993, ApJ, 419, L25

[47] Molnar, L.A., et al., 1995, ApJ, 438, 708

[48] Morris, M., Polish, N., Zuckerman, B., Kaifu, N., 1983, ApJ, 88, 1228

[49] Morris, M., 2007, in J. of Phys.: Conf. Series, Vol.54, preprint (astro-ph/0701050)

[50] Nore, C., Abid, M., and Brachet, M.E., 1997, Phys. Fluids, 9, 2644

[51] Oishi, J. S. and MacLow, M.-M., 2006, ApJ, 638, 281

[52] Oka, T., et al., 1998, ApJ, 493, 730

[53] Overton, N., Mills, R.J., and Coleman, P.J., 1993, J. Phys. B, 25, 557

[54] Pierce-Price, D., et al., 2000, ApJ, 545, L121

[55] Porter, T.A. and Strong, A.W., 2005, 29^{th} Int. Cosmic Ray Conf., 4, 77

[56] Ramaty, R. and Lingenfelter, R.E., 1979, Nature, 278, 127

[57] Ramaty, R., Stecker, F.W., and Misra, D., 1970, J. Geophys. Res., 75, 1141

[58] Rickett, B., et al., 2009, MNRAS, 395, 1391

[59] Rudaz, S. and Stecker, F.W., 1988, ApJ, 325, 16

[60] Schekochihin, A.A. and Cowley, S.C., 2007, in Magnetohydrodynamics: Historical Evolution and Trends, ed. S. Molokov, et al. (Berlin: Springer), 85 (arXiv:astro-ph/0507686v3)

[61] Schuecker, P., et al., 2004, A&A, 426, 387

[62] Skrbek, L., Niemela, J.J., and Donnelly, R.J., 2000, PRL, 85, 2973

[63] Spangler, S.R., 2007, ASP Conf. Ser., 365, 307

[64] Spangler, S.R. and Gwinn, C.R., 1990, ApJ, 353, L29

[65] Sperber, W., et al., 1992, Phys. Rev. Letters, 68, 3690

[66] Stecker, F. W., 1970, Ap&SS, 6, 377

[67] Tsuboi, M., Toshihiro, H., and Ukita, N., 1999, ApJS, 120, 1

[68] Veilleux, S., Cecil, G., and Bland-Hawthorn, J., 2005, ARAA, 43, 769

[69] Vogt, C. and EnBlin, T.A., 2005, A&A, 434, 67

[70] Walmsley, C.M., et al., 1986, A&A, 155, 129

[71] Weidenspointner, G., et al., 2008, Nature, 451, 159

[72] Werner, M.W., et al., 1988, ApJ, 333, 729

[73] Wommer, E., Melia, F., and Fatuzzo, M., 2008, MNRAS, 387, 987

[74] Young, J.S. and Scoville, N.Z., 1991, ARA&A, 29, 581

[75] Yusef-Zadeh, F. and Morris, M., 1987, ApJ, 94, 1178